

Hydrothermal alteration and short wavelength infrared (SWIR) characteristics of the Tongshankou porphyry-skarn Cu-Mo deposit, Yangtze craton, Eastern China



Jinsheng Han^{a,b,*¹}, Gaobin Chu^{a,1}, Huayong Chen^{a,c}, Pete Hollings^b, Siquan Sun^d, Mi Chen^d

^a Key Laboratory of Mineralogy and Metallogeny, Guangzhou Institute of Geochemistry, Chinese Academy of Sciences, Guangzhou 510640, China

^b Department of Geology, Lakehead University, 955 Oliver Road, Thunder Bay, Ontario P7B 5E1, Canada

^c State Key Laboratory of Geological Processes and Mineral Resources and School of Earth Sciences, China University of Geosciences, Wuhan 430074, China

^d Wuhan Institute of Geology and Mineral Resources, Wuhan 430205, China

ARTICLE INFO

Keywords:

Tongshankou deposit
Porphyry-skarn
SWIR
Chlorite
Eastern China

ABSTRACT

The Early Cretaceous Tongshankou Cu-Mo deposit is located in the eastern Yangtze craton and comprises both porphyry and skarn mineralization. The porphyry ore is hosted in a granodiorite porphyry with the skarn mineralization found along the contacts with the carbonate host rocks. Alteration in the porphyry mineralization can be divided into three stages: potassic alteration, phyllitic alteration and a carbonate stage, with phyllitic alteration associated with the main porphyry mineralization. No propylitic alteration is present at Tongshankou. The skarn-type alteration comprises five stages: early skarn stage, late skarn stage, oxide stage, quartz-sulfide stage and late vein stage. Short wave-length infrared (SWIR) analysis identified 15 hydrothermal minerals in the Tongshankou deposit, including illite, dickite, halloysite, phengite, talc, muscovite, saponite, gypsum, chlorite, prehnite, montmorillonite, serpentine, phlogopite, actinolite, kaolinite, with montmorillonite, illite and chlorite being the most common. SWIR parameters and the electron microprobe results of chlorites show that chlorites close to the mineralization center tend to be iron-rich and have high FeOH absorption position (Pos 2250 > 2251 nm). Consequently, chlorite may be a useful indicator mineral for mineralization in the Tongshankou deposit. Pos 2250 is not correlated to temperature as calculated using a chlorite geothermometer but does correlate with the iron contents of the chlorites. Our results show that the ore-forming fluids are Fe-rich in the proximity to the mineralization but Mg-rich towards the distal area. Unlike in other porphyry deposits the white mica shows no consistent variation in the Tongshankou deposit and cannot be used as vectors towards mineralization. The Fe-Mg-Al poor carbonate host rocks of the Tongshankou deposit restrict the development of a propylitic alteration zone. The Fe-Mg-Al host rocks also prevent Tschermak exchange in white mica ($(\text{Si}^{iv}(\text{Mg},\text{Fe})^{vi} \leftrightarrow \text{Al}^{iv}\text{Al}^{vi})$), making white mica Pos 2200 and Illite crystallinity (IC) randomly distributed. Our results show that SWIR spectroscopy of chlorite may be an applicable exploration tool in skarn-related hydrothermal systems.

1. Introduction

Shortwave infrared (SWIR) spectroscopy measured by portable infrared mineral analyzers cover wavelengths between 1300 and 2500 nm (Herrmann et al., 2001). In this range, light interacts with the molecular bonds of minerals (such as OH, H₂O, AlOH, CO₃, NH₄, MgOH and FeOH) to generate characteristic spectra (Thompson et al., 1999). SWIR can be used to investigate a wide range of SWIR-active minerals such as

phyllosilicates, hydroxylated silicates, sulfates, carbonates and ammonium-bearing minerals (Herrmann et al., 2001; Chang et al., 2011; Chang and Yang, 2012; Dalm et al., 2017). The SWIR method is non-destructive, simple to use, and allows for rapid data collection with minimal sample preparation at a relatively low cost (e.g., Thompson et al., 1999; Chang and Yang, 2012).

SWIR has recently been widely used for mineral mapping and exploration for various deposit types, including porphyry, epithermal and

* Corresponding author at: Key Laboratory of Mineralogy and Metallogeny, Guangzhou Institute of Geochemistry, Chinese Academy of Sciences, Guangzhou 510640, China.

E-mail address: hanjinsheng@gig.ac.cn (J. Han).

¹ These authors contributed equally.

volcanogenic massive sulfides (VMS; Herrmann et al., 2001; Yang et al., 2005; Chang et al., 2011; Harraden et al., 2013; Huang et al., 2017). In these deposits, alteration maps based on spectral variations were constructed to develop vectors to ore (Jones et al., 2005). For example, Chang et al. (2011) showed that in the Lepanto lithocap the alunite 1480 nm absorption peak shifts to higher wavelengths where the rock samples are closer to the intrusive centre. Similarly, Harraden et al. (2013) reported that the highest gold and Cu concentrations within the Pebble Porphyry Cu-Au-Mo deposit are coincident with low ALOH values associated with pyrophyllite and sericite alteration. In the Tuwu porphyry Cu deposits in Xinjiang, a trend of decreasing ALOH band wavelength (Pos 2200) for sericite towards mineralization was observed (Yang et al., 2005). In the Niancun ore district in Tibet, illite proximal to mineralization has higher IC (Illite crystallinity, > 1.6) and lower Pos 2200 (< 2203 nm) than more distal samples (Yang et al., 2012). Xu et al. (2017) have used high IC (> 2.1) and high Pos 2200 (> 2203 nm) as indicators of proximity to mineralization at the Zijianshan porphyry Cu-Au deposit in the Province of Fujian province, China. Herrmann et al. (2001) showed that white mica compositional variation can be effectively measured by SWIR spectrometry and can be effective vectors to ore in VMS deposits. Both SWIR and EPMA as well as LA-ICP-MS measurement have been carried out on chlorites of the Batu Hijau porphyry Cu-Au deposit in Indonesia. Results showed 1) chlorite crystallization temperature and radial distance from the mineralization center correlate well with each other (Wilkinson et al., 2015); 2) Porphyry deposits could be targeted by the chlorite Pos 2250, which is different between Mg-rich chlorite dominant in the inner propylitic zone and Fe-rich chlorite dominant further out (Neal et al., 2018).

The Middle-Lower Yangtze River metallogenic belt (MLYRB) is one of the most important Cu-Fe-Au-W-Mo skarn provinces in China, and is composed of several ore districts, including from west to east, Edong, Jiurui, Anqing, Luzong, Tongling, Ningwu and Ningzhen (Fig. 1; Pan and Dong, 1999). Most of these deposits formed in the Yanshanian and were associated with extensional structures (Pirajno and Zhou, 2015). The Edong ore district contains more than 50 porphyry-skarn and skarn deposits (Fig. 2; Xie et al., 2012), including the Tongshankou porphyry-skarn Cu-Mo deposit with 0.5 Mt Cu and 2000 t Mo, in the southwest of the Daye area (Li et al., 2008). Previous studies of Tongshankou deposit have mainly focused on the ore geology, age and isotopic geochemistry (Lv et al., 1992; Wang et al., 2004; Zhao et al., 2006; Li et al., 2008). In this study, detailed core logging and petrographic observation combined with systematic SWIR analysis have been conducted to develop a solid paragenesis of this complex porphyry-skarn deposit. Propylitic alteration is not well developed in the porphyry system of the Tongshankou deposit and most chlorites are observed in the skarn mineralization. SWIR characteristics of white micas and chlorite were evaluated to test the potential for vectoring to ore in Tongshankou. It also has implications for other similar deposits in the district.

2. Geological setting

2.1. Regional geology

The 560 km long MLYRB extends from Echeng in the west to Zhenjiang in the east (Lai et al., 2007; Ling et al., 2009; Fig. 1). The belt is situated between the southern margin of the North China Craton and Qinling-Dabie orogen and the northern margin of the Yangtze Craton. It

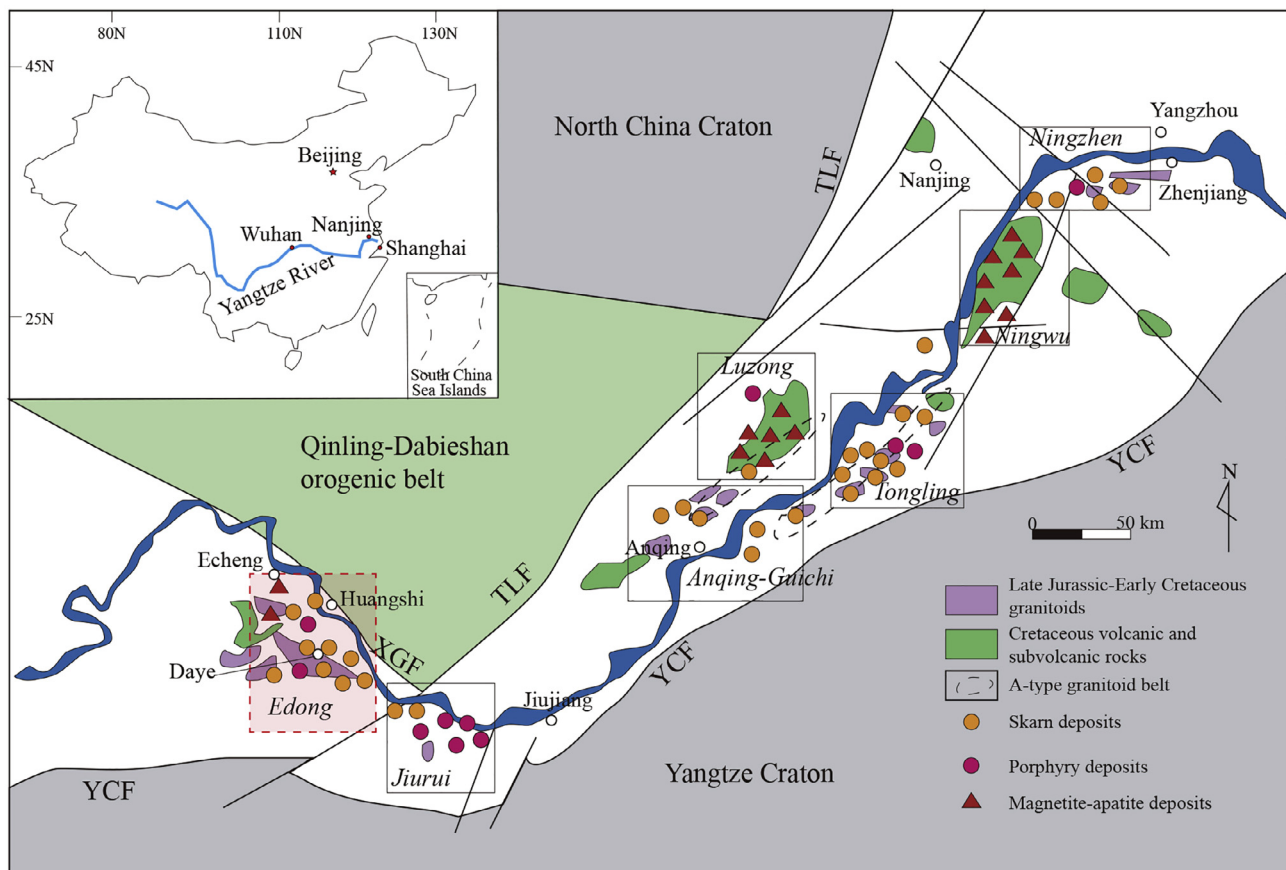


Fig. 1. Geological map of magmatic rocks and deposits in the Middle-Lower Yangtze River Valley Metallogenic Belt (modified from Chang et al., 1991). TLF: Tancheng-Lujiang fault, XGF: Xiangfan-Guangji fault, YCF: Yangxincang-Zhangzhou fault.

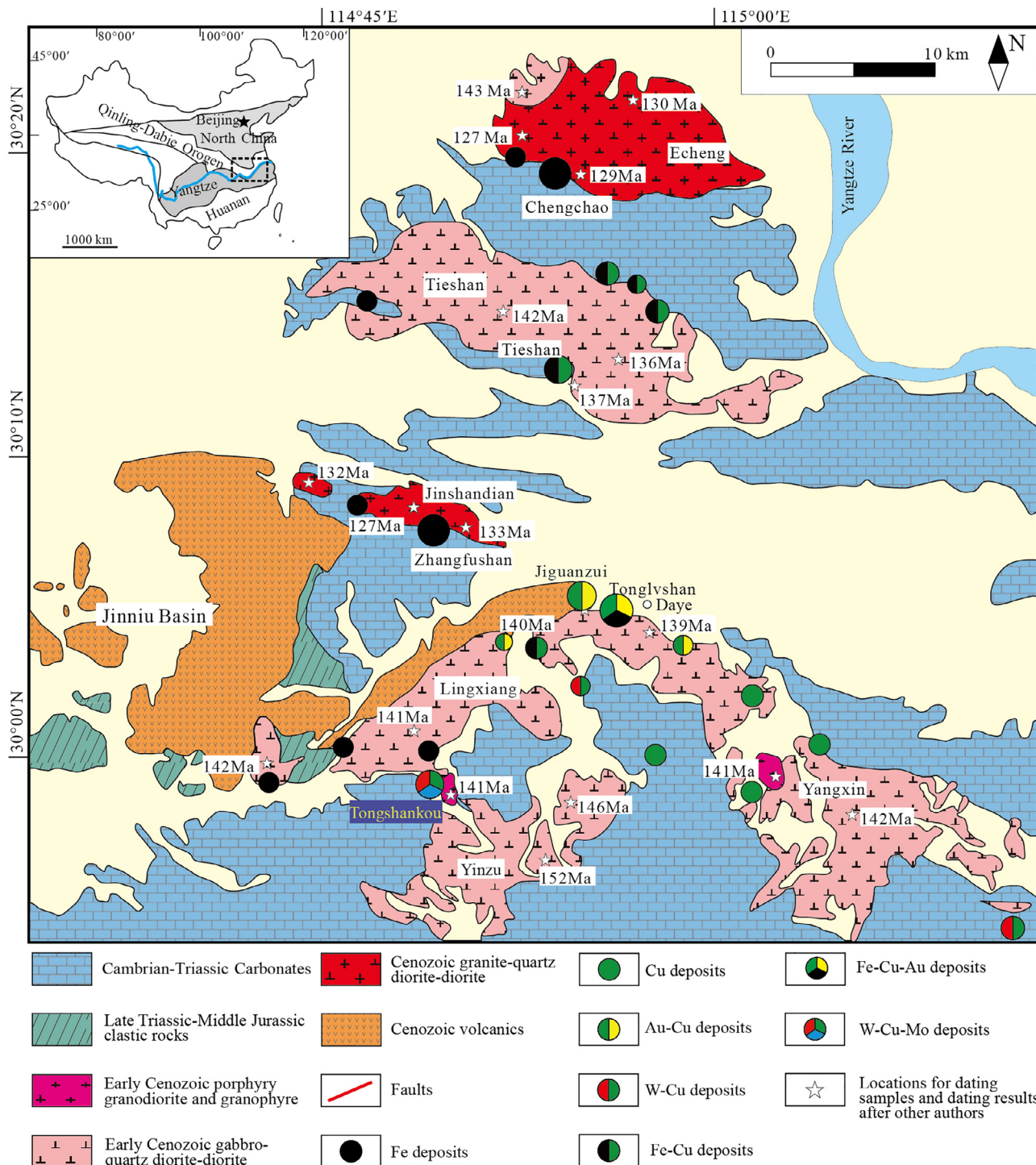


Fig. 2. Geological map of the Edong district, showing mineralization types and their emplacement age (modified from Xie et al., 2011). Different sizes of circles indicate the size of the deposit. Sample dating locations are from (Li et al., 2008, 2009; Xie et al., 2011, 2012).

is bounded by the Xiangfan-Guangji fault to the northwest, the Tan-Lu fault to the northeast and the Yangxing-Changzhou fault to the south (Fig. 1; Mao et al., 2006; Xie et al., 2015). The MLYRB is composed of Archean to Proterozoic metamorphic basement, Cambrian to Early Triassic sedimentary cover consisting of clastic rocks and carbonates,

and Middle Triassic to Cretaceous terrestrial clastic and volcanic rocks (Mao et al., 2006; Xie et al., 2012; Xie et al., 2015). The deep-seated Yangtze fracture zone, extending from Daye to Zhenjiang, was initiated in the Neo-Proterozoic and reactivated in the Late Jurassic to Late Cretaceous. Its formation was due to the convergence of the Yangtze

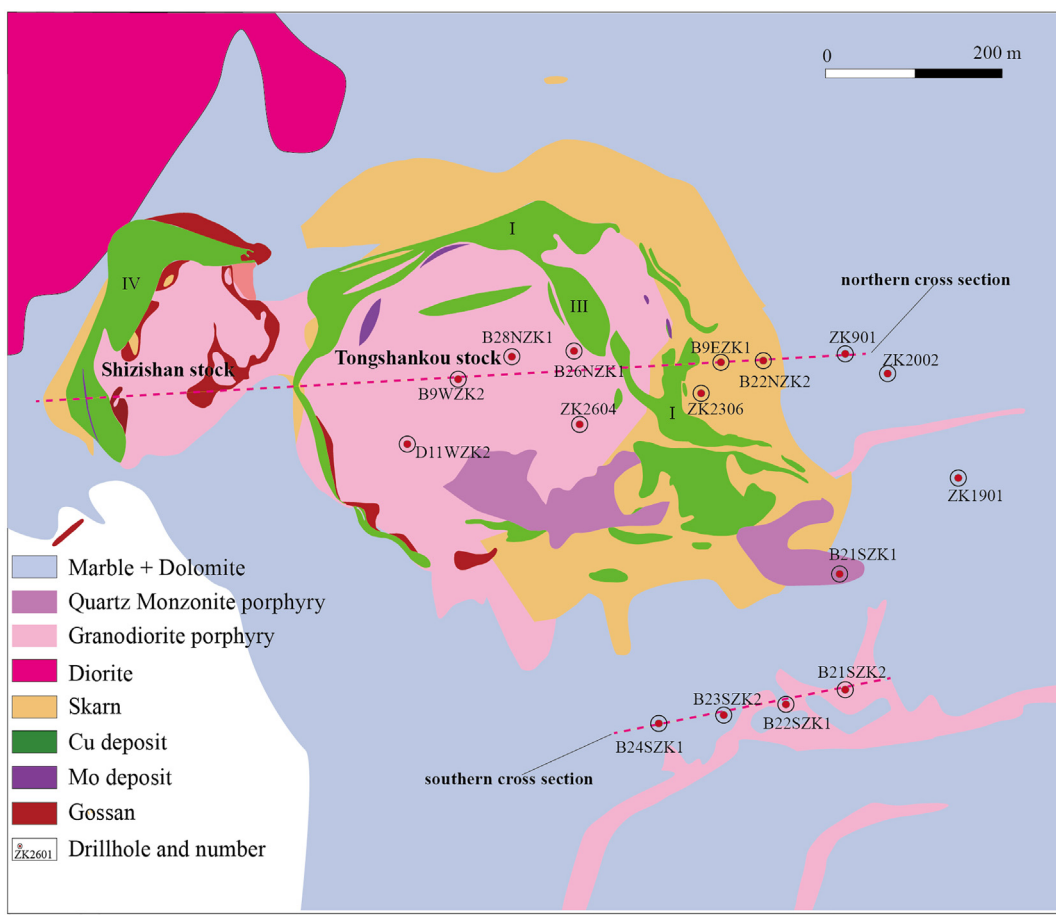


Fig. 3. Geological map of the Tongshankou deposit with the location of the northern and southern cross sections with respect to the drillhole locations (modified after Li et al., 2008).

Craton and the North China Craton, and may have played an important role in the metallogenesis of the MLYRB (Chang et al., 1991; Pan and Dong, 1999; Lai et al., 2007). Numerous Yanshanian granitoid intrusions, Upper Jurassic to Lower Cretaceous volcanic and volcaniclastic rocks and related ore deposits were formed after the final collision between the Yangtze Craton and the North China Craton in the Late Triassic (Pan and Dong, 1999; Lai et al., 2007; Ling et al., 2009).

The MLYRB contains more than 200 Cu-Au-Mo-Fe deposits, including 1) porphyry mineralization associated with the Jurassic-Cretaceous granitoid intrusions; 2) skarn mineralization located at the contacts between the Jurassic-Cretaceous intrusions and Late Paleozoic-Early Mesozoic carbonates and 3) minor stratiform massive sulphide orebodies in the Late Paleozoic-Early Mesozoic sedimentary rocks (Ling et al., 2009; Li et al., 2010; Zhou et al., 2015; Zhang et al., 2017).

The Edong ore cluster, located in the westernmost part of the MLYRB, hosts porphyry-skarn and skarn Cu-Fe-Au-W-Mo deposits in widespread Cambrian to Middle Triassic marine carbonates, clastic and flysch sequence (> 6000 m in thickness; Fig. 2; Xie et al., 2012, 2015, 2016; Xia et al., 2015). Six plutons (Echeng, Tieshan, Jinshanlidian, Lingxiang, Yinzu and Yangxin) and hundreds of small intrusions have been identified in the Edong district, ranging in an age from 150 to 120 Ma (Fig. 2; e.g., Li et al., 2009). The intrusion-related deposits in this area mainly occur around the Mesozoic intrusions (Xie et al., 2015).

2.2. Deposit geology

The Tongshankou deposit is closely related to the Tongshankou granodiorite which consists of the Shizishan stock (ca. 0.1 km²) in the west and the Tongshankou stock (ca. 0.33 km²) in the east (Fig. 3; Wang et al., 2004; Li et al., 2008). Both stocks show porphyry textures, with plagioclase (50–60%), hornblende (10–20%), quartz (10–15%) and minor apatite and titanite forming both phenocrysts and the groundmass. Microgranular enclaves are common in the granodiorite. Previous studies show the emplacement age of the Tongshankou stock to be about 140 Ma, within error of the Re-Os molybdenite ages (~143 Ma: Li et al., 2008). The country rocks consist of limestone and dolomitic limestone of the Lower Triassic Daye Formation (Lv et al., 1992; Shu et al., 1992; Li et al., 2008). The Tongshankou deposit consists of six Cu (Mo) ore bodies and numerous small Mo ore bodies, with No. I and IV being the largest (Fig. 3). The No. I ore body comprises ca. 60% of the total reserves at Tongshankou (Shu et al., 1992). The ore grade can be as high as 3.1% Cu and decreases away from the contact between the granodiorite and the carbonates (Li et al., 2008). The porphyry mineralization is only hosted in the granodiorite porphyry and skarn mineralization occurs at the contact of the granodiorite and the carbonates (Fig. 3). The small Mo ore bodies are all hosted in the granodiorite (Fig. 3). Porphyry mineralization is restricted to the No. III ore body

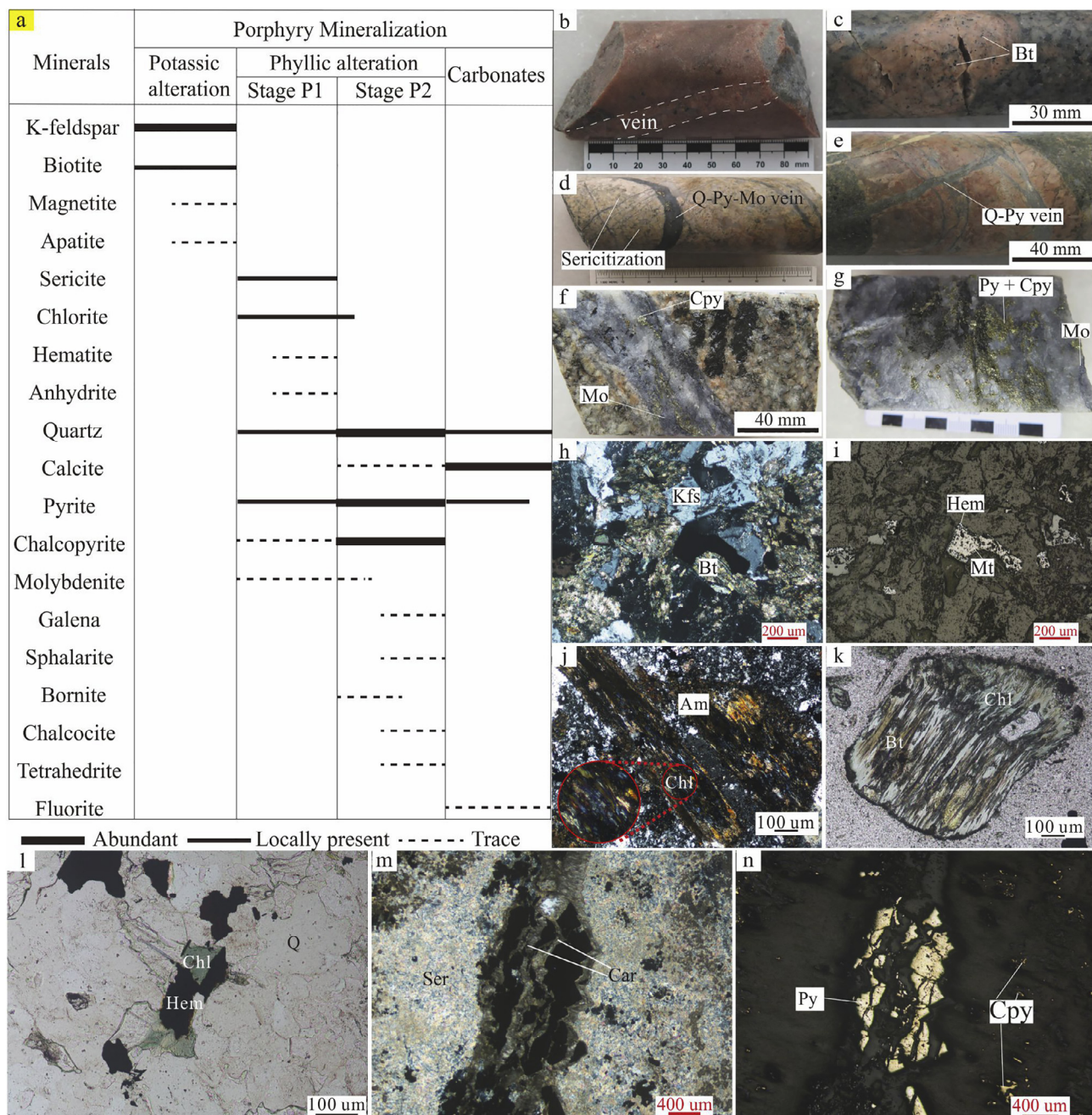


Fig. 4. Photographs, photomicrographs and paragenesis of the porphyry type alteration in the Tongshankou deposit. a) Paragenesis of the porphyry phase in the Tongshankou deposit; b) Potassic alteration of the porphyry granodiorite, showing the crosscutting relationships between different potassic veins; c) K-feldspar megacryst hosted in the porphyry granodiorite, containing some dark minerals such as biotite; d) Sericitization overprinting the early potassic alteration and crosscut by Q-Py-Mo vein; e) Potassic alteration crosscut by Q-Py vein; f) Q-Cpy-Mo vein crosscutting the potassic porphyry granodiorite; g) Py-Cpy-Mo-Q veins in the porphyry granodiorite; h) Photomicrographs of a k-feldspar megacryst, showing features of potassic alteration, Meanwhile, fine grained sericite could also be observed in the k-feldspar and biotite, showing that the potassic alteration was overprinted by phyllitic alteration. Under orthogonal polarized light; i) Photomicrographs of a k-feldspar megacryst, showing the coexistence of magnetite with biotite. There is a rim of hematite around the magnetite under visible reflected light; j) Photomicrographs showing carbonate veins crosscutting sericite. Under orthogonal polarized light; k) Photomicrographs showing carbonates veins crosscutting sericite, and the presence of pyrite with carbonates. Under reflected light. Bt: Biotite; Q: Quartz; Py: Pyrite; Mo: Molybdenite; Cpy: Chalcopyrite; Kfs: feldspar; Hem: Hematite; Ser: Sericite; Car: Carbonates.

with the remaining ore bodies consisting mainly of skarn type mineralization. Previous work has shown that the porphyry and skarn mineralization at Tongshankou resulted from the same hydrothermal

system based on contemporaneous phlogopite Ar-Ar ages and molybdenite Re-Os dating, as well as H-O-S isotopes (Lv et al., 1992; Li et al., 2008). These relationships have been used to show that the

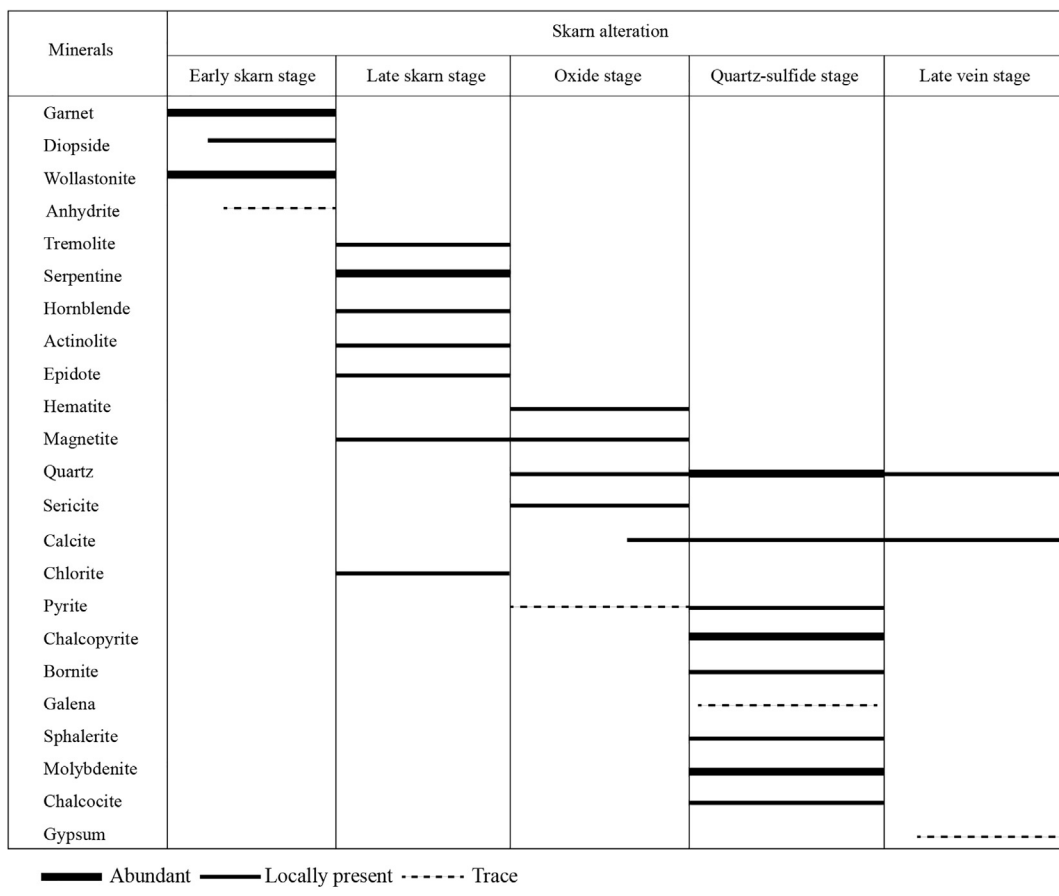


Fig. 5. Paragenesis of the skarn type alteration in the Tongshankou deposit.

porphyry granodiorite was responsible for the porphyry mineralization with skarn forming at the contact between the porphyry granodiorite and the carbonate host rock.

3. Paragenetic relationships

Based on visual and microscopic characteristics, combined with SWIR identification, a detailed paragenesis of the No. I ore body mineralization has been constructed (Figs. 4–6), which comprises two types of mineralization, the porphyry type and the skarn type.

3.1. Porphyry-type alteration and mineralization

The porphyry mineralization is generally restricted to the porphyry granodiorite. Some diorite enclaves could be occasionally observed in the porphyry granodiorite, especially in the deeper parts of the deposit.

Alteration in porphyry mineralization can be divided into three stages (Fig. 4a). 1) The first stage is dominated by potassic alteration that is ubiquitous in the center of the granodiorite. The occurrence of potassic alteration is dominated by vein type (Fig. 4b). Megacrystic potassic feldspar (Fig. 4c) coexisting with biotite and magnetite inclusions is common (Fig. 4c, h and i). Xu and Jiang (2017) proposed that the megacrystic K-feldspar represents the effects of potassic alteration from magmatic hydrothermal fluids based on in situ Sr-Pb isotopes. 2) The phyllitic alteration is most extensive at Tongshankou and can be divided into two substages (stage P1 and stage P2) with chalcopyrite

mainly observed in the second substage (stage P2): a) Sericitization of the potassic feldspar and biotite (Fig. 4h) with veins often < 1 cm and little chalcopyrite, showing the potassic alteration overprinted by phyllitic alteration. Quartz-pyrite-molybdenite and quartz-pyrite veins crosscut the potassically altered granodiorite (Fig. 4d and e). Chloritization of magmatic hornblende and biotite could be observed (Fig. 4j and k). Some quartz-chlorite-hematite veins crosscut the porphyry granodiorite (Fig. 4l); b) In this substage, veins are much wider and often >>1 cm. Chalcopyrite is abundant and commonly found in quartz-molybdenite and quartz-pyrite veins (Fig. 4f and g). This stage is most economically important for the porphyry mineralization. 3) The late carbonate stage comprises carbonate veins that coexist with pyrite and minor quartz crosscutting the earlier sericite alteration (Fig. 4m and n). Propylitic alteration which is common in other typical porphyry deposits was rarely observed.

3.2. Skarn-type alteration and mineralization

At the contact between the granodiorites and the carbonates, the mineralization changes into skarn type. The detailed paragenesis of skarn alteration and mineralization is displayed in Fig. 5. The skarn mineralization can be subdivided into five stages. 1) The early skarn stage consists of garnet and wollastonite at the contact with limestone. Two kinds of garnet were observed, a euhedral type with well-developed zoning (Fig. 6a1, a2, b, f and g) and a massive, poorly crystallized type (Fig. 6c1 and c2). The massive garnet is spatially associated with

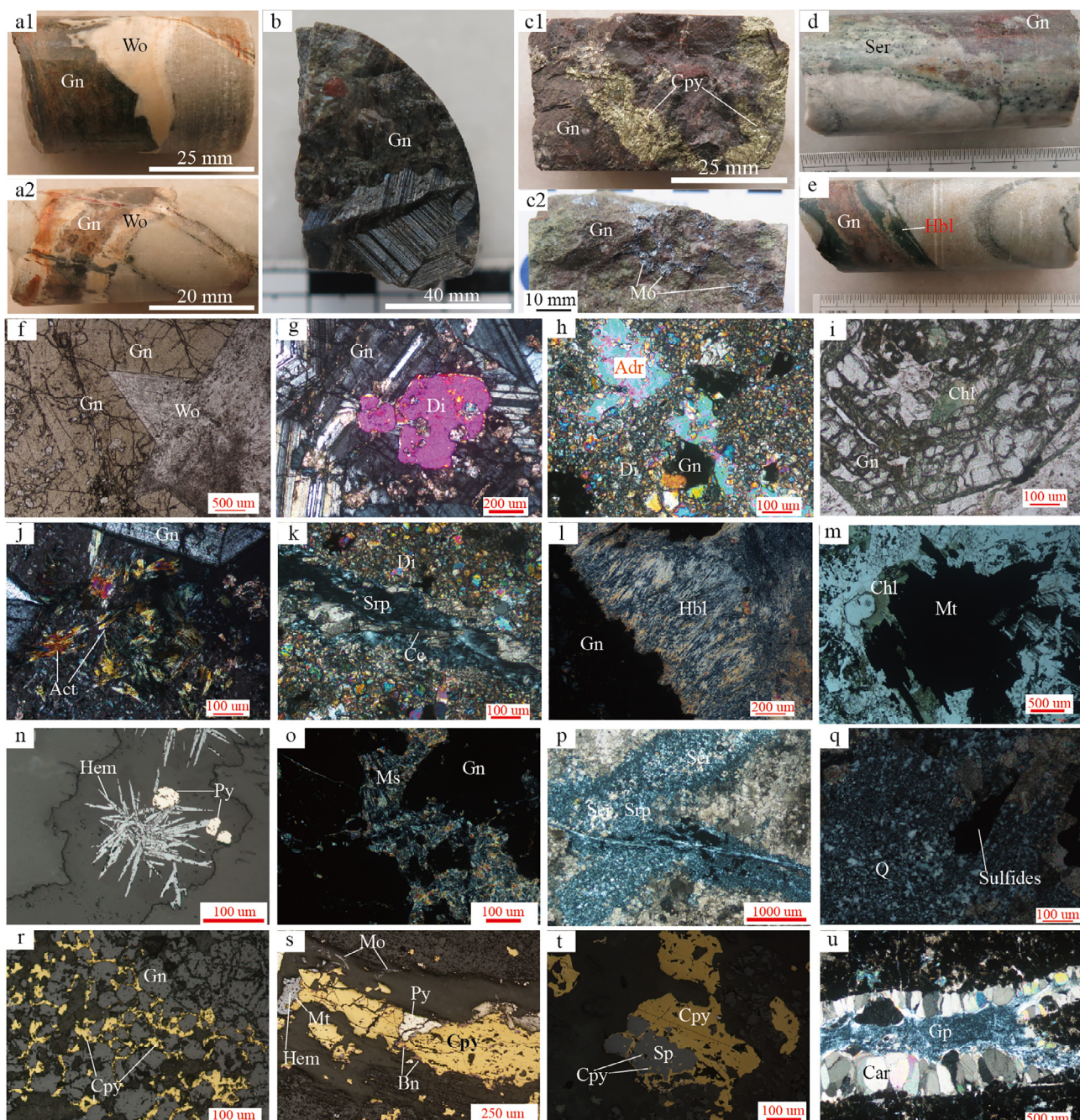


Fig. 6. Photographs and photomicrographs of the skarn mineralization in the Tongshankou deposit. a1) Coexistence of zoned garnet with wollastonite; a2) Coexistence of garnet veins with wollastonite; b) Garnet with obvious zoning; c1) Massive garnet with chalcopyrite; c2) Massive garnet with molybdenite; d) Garnet replaced by sericitic; e) Garnet replaced by hornblende; f) Photomicrograph showing the coexistence of garnet and wollastonite in plain polarized light; g) garnet with diopside in orthogonal polarized light; h) Photomicrograph showing the replacement of garnet by anhydrite in orthogonal polarized light; i) Photomicrograph chlorite filling in the interstices of garnet in orthogonal polarized light; j) Actinolite filling the interstices of garnet in orthogonal polarized light; k) Photomicrograph showing the diopside cut by serpentine and serpentine crosscut by a calcite vein in orthogonal polarized light; l) Hornblende in the interstices of garnet in orthogonal polarized light; m) Photomicrograph of chlorite and magnetite in plain polarized light; n) Hematite with minor pyrite in reflected light; o) Muscovite in the interstices of garnet; p) Photomicrographs showing the replacement of serpentine by sericitic in plain polarized light; q) Coexistence of quartz with sulfides in orthogonal polarized light; r) Chalcopyrite veins filling the interstices of garnet; s) Coexistence of molybdenite, pyrite, chalcopyrite and bornite, with minor magnetite and hematite; t) Coexistence of chalcopyrite and sphalerite. Exsolution textures can be observed in the sphalerite; u) late carbonate vein crosscut by gypsum veins in orthogonal polarized light. Gn: Garnet; Wo: Wollastonite; Cpy: Chalcopyrite; Mo: Molybdenite; Ser: Sericitic; Hb: Hornblende; Di: Diopside; Adr: Anhydrite; Chl: Chlorite; Act: Actinolite; Srp: Serpentine; Cc: Calcite; Hem: Hematite; Py: Pyrite; Ms: Muscovite; Q: Quartz; Sp: Sphalerite; Car: Carbonate; Gp: Gypsum.

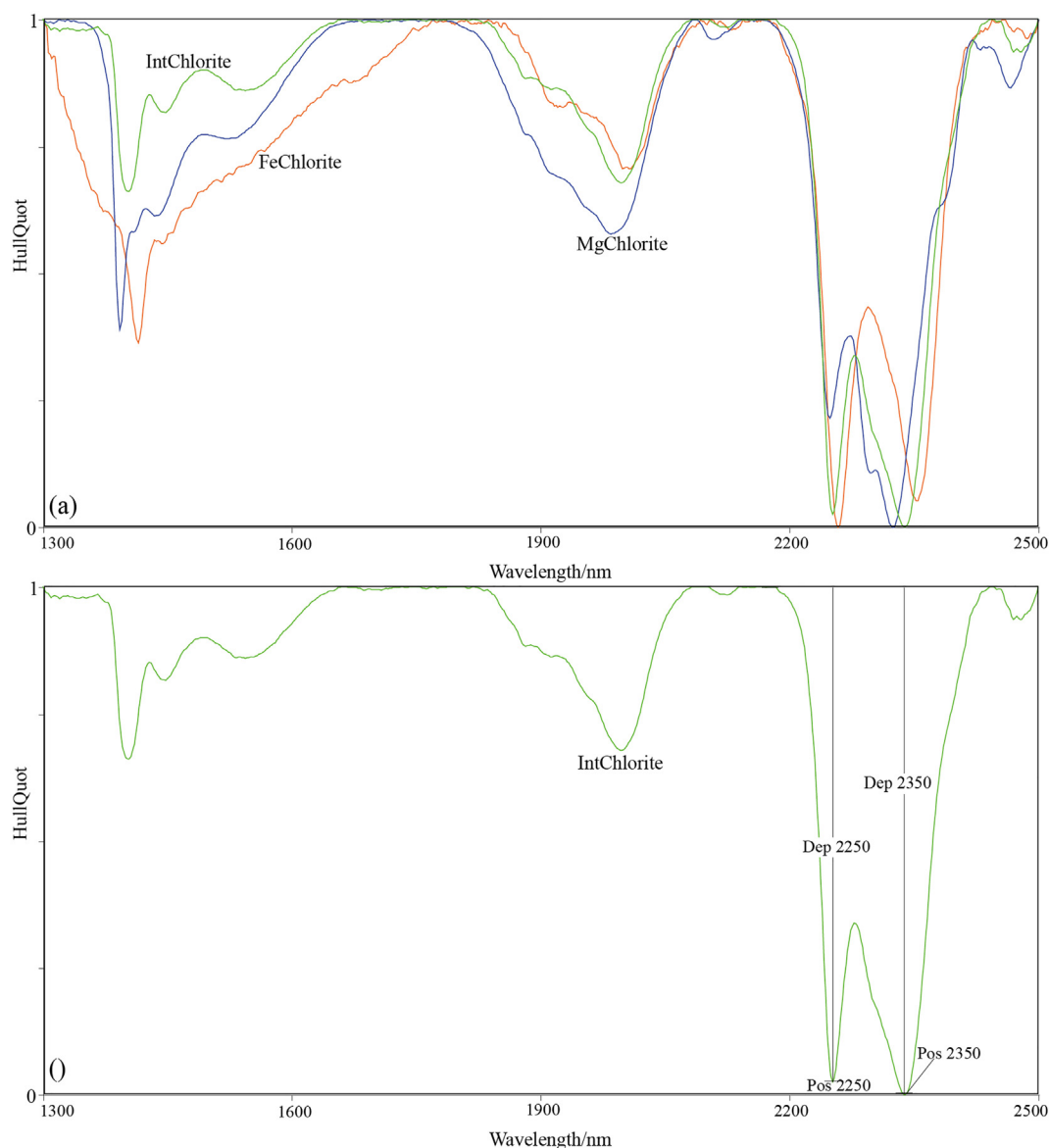


Fig. 7. (a) SWIR characteristics of chlorite (according to the TSG library); (b) Using IntChlorite as an example, the primary SWIR features used in this study are the Pos 2250, Dep 2250, Pos 2350, and Dep 2350.

mineralization (Fig. 6c1 and c2). Diopside and minor anhydrite coexist with the garnet (Fig. 6g and h). 2) In the late skarn stage, the garnets are partly replaced by serpentine, actinolite, hornblende and chlorite (Fig. 6e, i-l). Magnetite coexists with the hydrous skarn minerals (Fig. 6m). 3) The oxide stage is characterized by the occurrence of hematite and muscovite (Fig. 6n and o) with minor pyrite occasionally coexisting with the hematite (Fig. 6n). The serpentine was partially replaced by sericite (Fig. 6p). 4) The quartz-sulfide stage hosts the majority of Cu-Mo mineralization in the Tongshankou deposit. Chalcopyrite commonly coexists with molybdenite, bornite and sphalerite (Fig. 6c1, c2, q-t). 5) The late vein stage mainly comprise quartz and carbonate veins. Locally, vein-type gypsum crosscut the carbonate.

4. SWIR analysis

4.1. SWIR background

Shortwave infrared (SWIR) spectroscopy can measure reflectance in the short wavelength infrared range of 1300–2500 nm based on interaction between light and molecular bonds of minerals (Herrmann et al., 2001; Chang et al., 2011; Chang and Yang, 2012; Dalm et al., 2017). It is especially useful to identify phyllosilicates based on their characteristic spectra, among which, chlorite and white mica are most widely used as exploration vectors in hydrothermal deposits (e.g. Herrmann et al., 2001; Neal et al., 2018).

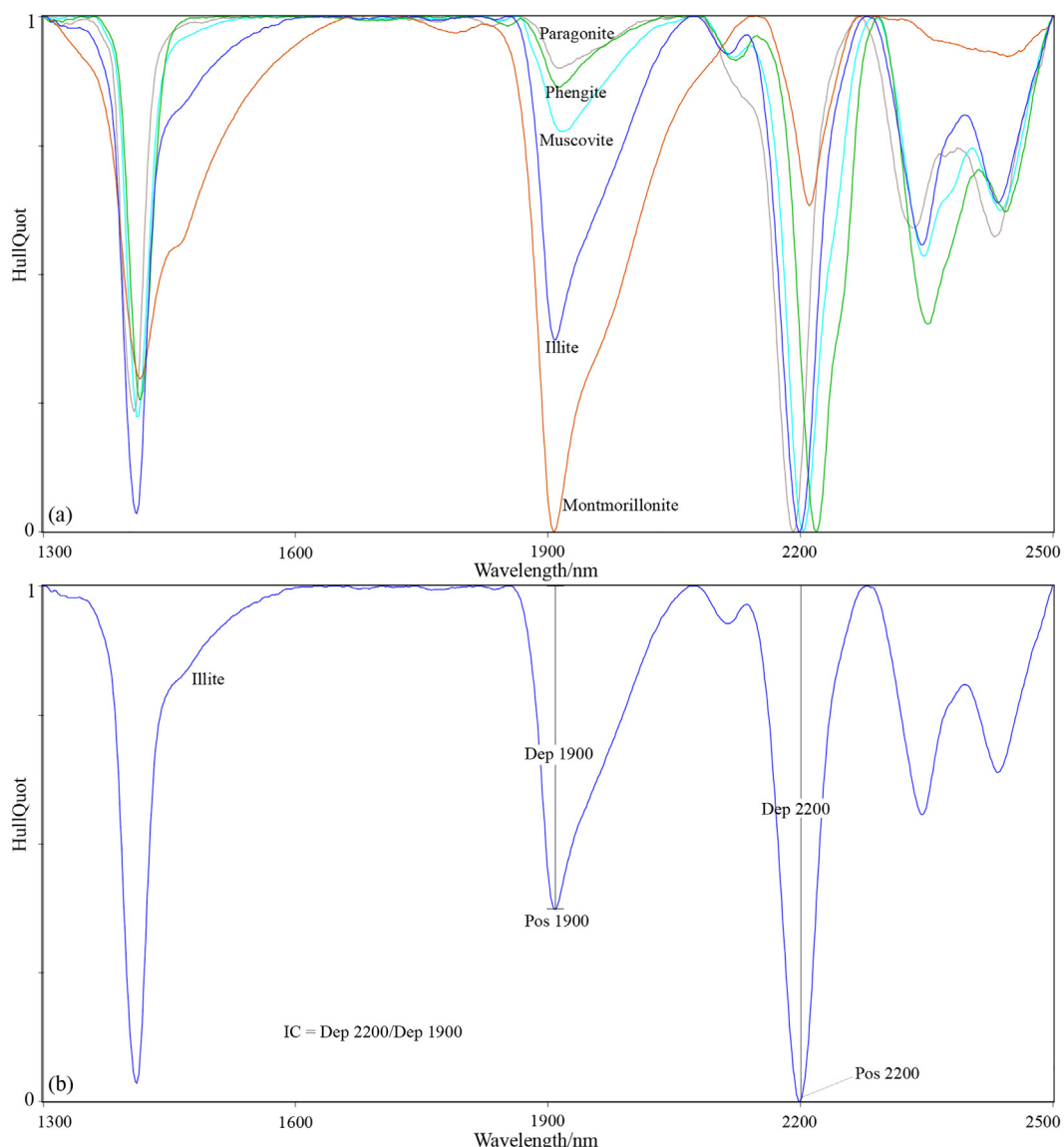


Fig. 8. (a) SWIR characteristics of white mica (according to the TSG library); (b) Using illite as an example, the primary SWIR features used in this study are the Pos 1900, Dep 1900, Pos 2200, and Dep 2200.

Chlorite is an umbrella term that usually refers to clinochlore, chamosite, and/or a solid solution between these two end members (Dalm et al., 2014). Chlorite group has diagnostic FeOH and MgOH absorption features centered around ~2250 nm and ~2350 nm (i.e., Pos 2250, Depth 2250, Pos 2350, Dep 2350, Fig. 7; Herrmann et al., 2001; Dalm et al., 2014). They can be divided into three sub-groups according to the reference library of the TSG, i.e., FeChlorite, MgChlorite and IntChlorite (Fig. 7). Neal et al. (2018) found that both the chlorite Pos 2250 and Pos 2350 show decreasing trend from the center of mineralization away in the Batu Hijau porphyry Cu-Au deposit in Indonesia.

White mica is an umbrella term which includes muscovite, paragonite, illite, and/or any coexisting occurrence of these minerals (Dalm et al., 2014). White mica has a sharp absorption in the AlOH band at ~2200 nm (Pos 2200), weaker AlOH features near 2340 and 2440 nm

and various H₂O features at ~1900 nm (Pos 1900; Fig. 8; Herrmann et al., 2001). The absorption depth at ~2200 nm and 1900 nm are referred to here as Depth 2200 and Depth 1900. The “Illite crystallinity” (IC), calculated using the ratio of Depth 2200/Depth 1900, is commonly used to measure the crystallinity of illite and has been shown to positively correlated with the formation temperature of white mica (Chang et al., 2011). The most frequently used SWIR parameters for white mica are Pos 2200 and IC (Herrmann et al., 2001; Chang et al., 2011; Yang et al., 2012; Laakso et al., 2016). For example, in the Tuwu porphyry Cu deposits in Xinjiang, a trend of decreasing AlOH band wavelength (Pos 2200) for sericite towards mineralization was observed (Yang et al., 2005). In the Niancun ore district in Tibet, illite proximal to mineralization has higher IC (> 1.6) and lower Pos 2200 (< 2203 nm) than more distal samples (Yang et al., 2012).

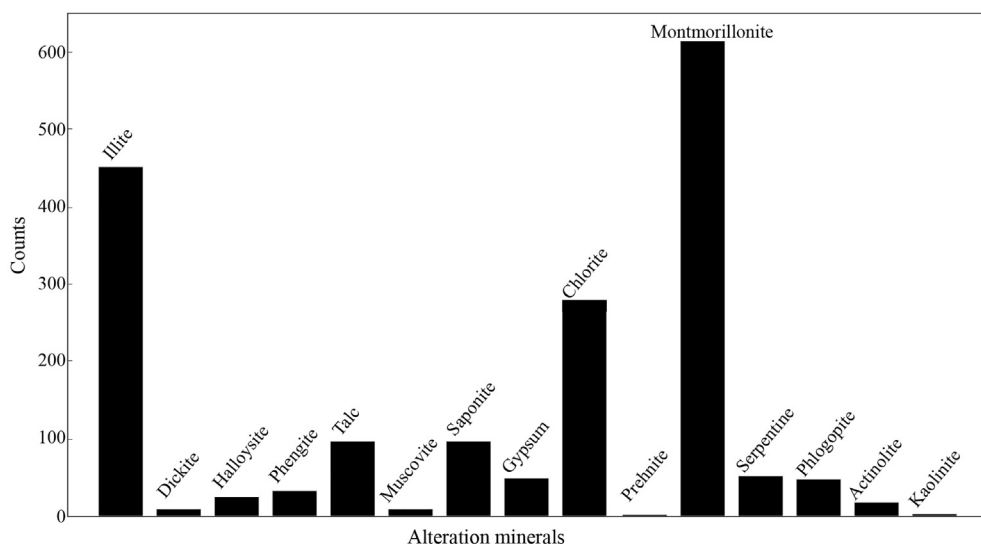


Fig. 9. Abundance of alteration minerals identified by TerraSpec at the Tongshankou deposit. Counts for the y-axis refers to the number of times a mineral name is reported. There are 3380 results in this figure.

4.2. Data collection methods

As stated earlier, the No. I ore bodies were dominated by skarn mineralization. The lack of propylitic alteration in the Tongshankou means that any chlorite SWIR features is tracking changes in skarn alteration only. So even though porphyry alteration could be observed in the drillholes, all the samples are used to reflect vectors to skarn mineralization. Samples were commonly taken at 10 m intervals within each drillhole, but when the alteration became visually intense, more samples will be collected and the intervals will be less. 1335 samples were collected from 16 drillholes (Fig. 3). All the samples were washed and dried to exclude the effects of dust and moisture. Two or three analyses at different spots on the sample were carried out and zones with sulfides were avoided where possible to increase signal-to-noise ratios. 3725 SWIR spectra were obtained from core samples with a TerraSpec 4 Hi-Res made by Analytical Spectral Devices Inc. The TerraSpec has a 2.5-cm-diameter circular window. We set it to 10 s for one analysis following the method of Chang and Yang (2012). The TerraSpec unit was calibrated with a Spectralon® disk every 20 min. The spectral files were splice-corrected via the ViewSpecPro software and converted to ASCII format. The spectra were manually interpreted with assistance of “The Spectral Geologist” (TSG 3) according to the features of each spectrum compared with a reference library in the software. 345 of the 3725 measurements were discarded due to low signal to noise ratios. The remaining spectra were hull corrected in order to minimize the interference effects of background absorption (Laakso et al., 2016). The diagnostic absorption features of OH, H₂O, CO₃, NH₄, AlOH, FeOH and MgOH molecular bonds have been identified by Thompson et al. (1999), allowing for the identification of phyllosilicates, carbonates, OH-bearing silicates and sulfates. Parameters such as absorption position and the absorption depth of minerals (such as such as Pos 2250, Dep 2250 of chlorites or Pos 2200 and IC of white mica) were extracted using the TSG software. An average value for each parameter from two or three spot analyses for each sample were used.

As samples with particular hydrothermal minerals may not be so dense, the mapping of spatial distribution of useful SWIR parameters (such as Pos 2250, Dep 2250 of chlorites or Pos 2200 and IC of white

mica) of certain hydrothermal minerals on certain cross section may not be obvious. So some certain interpolation technique may be adopted. Among so many interpolation methods, kriging interpolation technique was chosen because this method is based on a model of stochastic spatial variation that fits well with reality and thus often realistically reflects the natural world (Oliver and Webster, 1990). Contour maps of certain data were displayed via Surfer 10 using a kriging interpolation method.

Electron microprobe analyses (EMPA) of some chlorite grains from both porphyry and skarn samples which look large enough and homogenous were performed using a JEOL JXA 8230 electron microprobe at the Key Laboratory of Mineralogy and Metallogenesis, GIG-CAS, Guangzhou, China. The operating conditions were as follows: 15 kV accelerating voltage, 20nA beam current. The beam diameter was 1 μm. Major element compositions of multiple spots on multiple grains were acquired. Most chlorites are not big enough to be analyzed by EMPA. A total 44 EMPA analyses were obtained from the southern cross section, with 2–6 spots analyses acquired from each sample on 2–3 separate chlorite grains. Mineral formulae were calculated on the basis of 28 oxygens for chlorite. The mineral cations were then compared to the average SWIR features of the same sample.

5. Results

5.1. Mineral identification by SWIR

Because the main host rocks are marble and/or dolomites, any carbonates (mainly calcite, dolomite, ankerite) identified by SWIR were not considered in this study. Spectra of samples with high sulfide contents were also excluded as they typically yield noisy absorption spectra (without recognizable absorption features; Hunt, 1979; Clark et al., 2007). As a result, 345 spectra were discarded. Based on SWIR characteristics of the 3380 SWIR spectra from the 1335 Tongshankou drill core samples, 15 hydrothermal minerals were identified in the Tongshankou deposit, including illite, dickite, halloysite, phengite, talc, muscovite, saponite, gypsum, chlorite, prehnite, montmorillonite, serpentine, phlogopite, actinolite, kaolinite. Of these, montmorillonite,

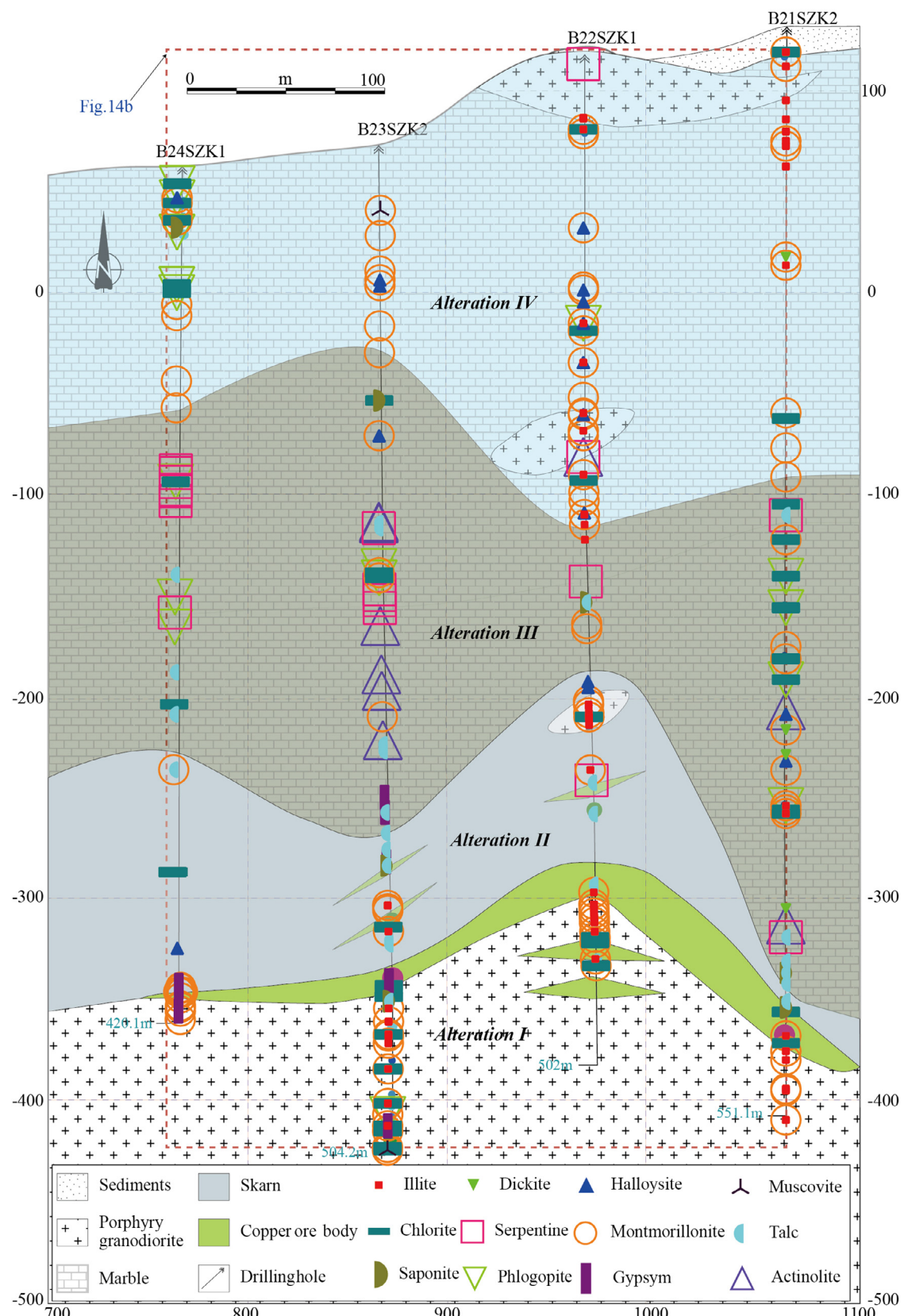


Fig. 10. Alteration zones based on field observations and the distribution of alteration minerals identified by TerraSpec in the southern cross section. Alteration I: mainly distributed in the porphyry granodiorite with alteration mineral assemblage consisting of chlorite + montmorillonite + illite ± gypsum. Alteration II: intensely altered and mainly distributed in the contact between the porphyry granodiorite and the carbonate rocks with the alteration mineral assemblage consisting of garnet + diopside + wollastonite + saponite + chlorite + montmorillonite + illite. Alteration III: distributed in the carbonate rocks and weakly altered. The alteration mineral assemblage consist of serpentine + phlogopite + chlorite + actinolite + saponite + talc. Alteration IV: distributed in the carbonate rocks with very weak alteration. The alteration mineral assemblage mainly consist of secondary montmorillonite + halloysite.

Table 1

SWIR results of the chlorites in the northern cross section of the Tongshankou deposit.

Samples	Mineral 1	Mineral 2	Mineral 3	Pos 2250	Dep 2250	Pos 2335	Dep 2335	Remarks	Depth	x	y
B9WZK2-8	Montmorillonite	IntChlorite		2246.80	0.05	2336.68	0.06	2 data average	-6.39	38580437.31	3320450.39
B9WZK2-19	Illite	IntChlorite		2245.66	0.08	2339.27	0.12	3 data average	-103.64	38580431.89	3320450.12
B9WZK2-24	Montmorillonite	IntChlorite		2241.56	0.05	2334.95	0.06		-147.96	38580429.18	3320450.00
B9WZK2-25	Montmorillonite	Illite	MgChlorite	2243.08	0.05	2332.14	0.07		-167.51	38580427.91	3320449.95
B9WZK2-28	Montmorillonite	Illite	MgChlorite	2242.71	0.07	2328.86	0.08		-211.03	38580425.26	3320449.86
B9WZK2-29	Montmorillonite	MgChlorite	IntChlorite	2246.02	0.04	2333.76	0.06	3 data average	-223.41	38580424.54	3320449.83
B9WZK2-39	Montmorillonite	IntChlorite		2250.16	0.06	2334.78	0.09		-265.78	38580422.00	3320449.74
B9WZK2-42	Montmorillonite	IntChlorite		2247.08	0.12	2334.95	0.15	3 data average	-340.99	38580417.33	3320449.64
B9WZK2-43	Montmorillonite	IntChlorite		2247.86	0.08	2336.45	0.11	3 data average	-357.06	38580416.33	3320449.68
B9WZK2-45	Montmorillonite	IntChlorite		2245.83	0.07	2331.58	0.09	2 data average	-368.69	38580415.61	3320449.72
B9WZK2-47	Montmorillonite	Illite	IntChlorite + MgChlorite	2244.61	0.07	2332.70	0.11	3 data average	-391.39	38580414.19	3320449.80
B9WZK2-52	Montmorillonite	IntChlorite		2244.38	0.08	2337.43	0.12	2 data average	-472.03	38580409.15	3320450.36
B9EJK1-8	Montmorillonite	IntChlorite		2251.66	0.06	2336.41	0.09	2 data average	-353.31	38580857.22	3320477.29
B9EJK1-12	Montmorillonite	IntChlorite		2247.06	0.07	2342.26	0.09		-387.39	38580855.97	3320477.20
B9EJK1-13	Montmorillonite	IntChlorite		2242.46	0.07	2340.39	0.09		-390.98	38580855.83	3320477.19
B9EJK1-14	Montmorillonite	Illite	IntChlorite	2250.83	0.11	2338.27	0.16		-401.18	38580855.46	3320477.17
B9EJK1-15	Montmorillonite	Illite	IntChlorite	2242.40	0.07	2339.18	0.08	2 data average	-407.47	38580855.22	3320477.15
B9EJK1-16	Montmorillonite	Illite	IntChlorite	2248.69	0.12	2339.11	0.18		-413.52	38580854.99	3320477.13
B9EJK1-23	Montmorillonite	IntChlorite		2246.73	0.06	2337.03	0.09		-468.33	38580852.94	3320476.99
B9EJK1-25	Montmorillonite	Illite	IntChlorite	2245.75	0.06	2344.17	0.06		-494.11	38580851.97	3320476.92
B9EJK1-26	Montmorillonite	Illite	IntChlorite	2249.68	0.05	2339.92	0.06		-502.21	38580851.66	3320476.90
B9EJK1-68	IntChlorite			2257.21	0.11	2341.15	0.14	3 data average	-226.99	38580859.76	3320477.47
B9EJK1-74	Calcite	IntChlorite		2259.72	0.06	2331.84	0.07		-237.14	38580859.72	3320477.46
B9EJK1-82	Calcite	FeChlorite		2256.15	0.07	2349.91	0.06		-267.75	38580859.63	3320477.46
B9EJK1-83	calcite	IntChlorite		2260.21	0.07	2341.20	0.10	3 data average	-269.75	38580859.62	3320477.46
B9EJK1-90	Calcite	MgChlorite		2258.51	0.05	2334.45	0.05	2 data average	-299.49	38580859.19	3320477.43
B9EJK1-92	Calcite	IntChlorite		2250.98	0.04	2334.77	0.04	3 data average	-309.18	38580858.83	3320477.40
B22NZK2-42	Calcite	IntChlorite		2259.02	0.10	2339.13	0.17	2 data average	-207.13	38580929.04	3320474.72
B22NZK2-43	Saponite	FeChlorite		2252.87	0.04	2316.54	0.07		-208.85	38580929.05	3320474.70
B22NZK2-44	MgChlorite			2249.07	0.03	2316.03	0.07		-209.85	38580929.06	3320474.69
B22NZK2-45	Calcite	IntChlorite		2250.66	0.21	2341.79	0.18	2 data average	-212.51	38580929.07	3320474.67
B22NZK2-50	Calcite	Montmorillonite	MgChlorite	2243.32	0.17	2336.35	0.22		-226.75	38580929.14	3320474.54
B22NZK2-55	Calcite	IntChlorite		2251.10	0.10	2339.90	0.22		-247.15	38580929.25	3320474.36
B22NZK2-66	Calcite	IntChlorite		2255.45	0.06	2333.68	0.08	2 data average	-292.85	38580929.48	3320473.93
B22NZK2-70	IntChlorite			2252.98	0.11	2342.00	0.14	2 data average	-296.15	38580929.50	3320473.89
B22NZK2-82	Montmorillonite	IntChlorite		2250.46	0.08	2336.49	0.11		-357.22	38580929.80	3320473.12
B22NZK2-104	IntChlorite			2249.30	0.05	2339.03	0.06	3 data average	-510.91	38580932.38	3320472.82
B22NZK2-105	IntChlorite			2252.20	0.05	2350.45	0.06		-511.71	38580932.40	3320472.83
B22NZK2-106	MgChlorite			2245.06	0.03	2325.66	0.06	2 data average	-516.68	38580932.50	3320472.88
B22NZK2-108	Calcite	MgChlorite		2248.61	0.03	2327.42	0.06		-527.68	38580932.73	3320472.99
B22NZK2-112	IntChlorite			2257.75	0.03	2333.44	0.04	2 data average	-541.30	38580933.02	3320473.13
B22NZK2-113	IntChlorite			2257.33	0.07	2336.59	0.11	3 data average	-539.70	38580932.98	3320473.11
B22NZK2-118	Calcite	IntChlorite		2260.04	0.07	2338.66	0.12		-558.81	38580933.38	3320473.31
B22NZK2-119	Calcite	IntChlorite		2259.03	0.08	2339.53	0.11	3 data average	-561.01	38580933.43	3320473.33
B22NZK2-123	MgChlorite			2252.65	0.07	2329.70	0.16	3 data average	-570.90	38580933.64	3320473.43
B22NZK2-124	IntChlorite			2262.35	0.05	2333.32	0.12	2 data average	-575.00	38580933.72	3320473.47
B22NZK2-125	IntChlorite			2253.20	0.04	2332.62	0.07	2 data average	-577.99	38580933.78	3320473.50
B22NZK2-126	IntChlorite			2260.66	0.11	2340.06	0.19		-580.59	38580933.84	3320473.53
B22NZK2-129	MgChlorite	Montmorillonite		2243.02	0.02	2319.22	0.04	2 data average	-603.29	38580934.28	3320473.58
B22NZK2-130	MgChlorite	Montmorillonite		2247.45	0.02	2320.37	0.06		-619.99	38580934.60	3320473.60
B22NZK2-135	Calcite	IntChlorite		2265.04	0.13	2339.12	0.21		-643.40	38580935.05	3320473.63
B22NZK2-137	IntChlorite			2259.54	0.06	2338.77	0.10	2 data average	-650.08	38580935.18	3320473.64
ZK901-55	MgChlorite	Talc		2242.08	0.03	2313.16	0.05		-317.93	3320564.03	3320490.90
ZK901-80	IntChlorite	Actinolite		2253.47	0.06	2331.82	0.10	2 data average	-736.12	38580973.33	3320492.08
ZK901-81	Montmorillonite	IntChlorite		2247.79	0.06	2337.26	0.06	2 data average	-739.01	38580973.13	3320492.09
ZK901-82	Montmorillonite	IntChlorite		2247.66	0.12	2338.61	0.17		-741.90	38580972.93	3320492.10
ZK901-85	Montmorillonite	MgChlorite	IntChlorite	2251.97	0.05	2330.33	0.10	3 data average	-788.70	38580969.85	3320492.26
ZK901-90	Montmorillonite	IntChlorite		2243.25	0.11	2358.66	0.10		-856.79	38580965.98	3320492.48

illite and chlorite, were the most common (Fig. 9). White mica and chlorite are the most common alteration minerals identified by SWIR, and they are also widespread in hydrothermal systems. Some previous works concentrating on white mica and chlorite for exploration have been published (e.g. Herrmann et al., 2001; Wilkinson et al., 2015; Neal et al., 2018). So we focused on the spectra of these two minerals on two cross sections which contain the most drillholes, i.e., the northern cross

section (containing drillholes B9WZK2, B09EJK1, B22NZK2, ZK901) and the southern cross section (containing drillholes B21SZK2, B22SZK1, B23SZK2, B24SZK1; Fig. 3), to illustrate the spatial distribution of alteration minerals. A SWIR mineralogy cross-section could be easily built (Fig. 10).

Table 2

SWIR results of chlorites in the southern cross section of the Tongshankou deposit.

Samples	Mineral 1	Mineral 2	Mineral 3	Pos 2250	Dep 2250	Pos 2335	Dep 2335	Remarks	Depth	x	y
B21SZK2-3	Montmorillonite	Illite	IntChlorite	2242.48	0.10	2341.06	0.11		117.81	38581061.82	3319951.32
B21SZK2-25	Calcite	MgChlorite		2248.86	0.13	2332.17	0.23		-62.48	38581061.82	3319954.53
B21SZK2-29	MgChlorite			2248.80	0.23	2321.30	0.29		-104.60	38581061.82	3319955.77
B21SZK2-31	Montmorillonite	FeChlorite		2244.29	0.20	2323.43	0.35		-122.09	38581061.82	3319956.29
B21SZK2-32	MgChlorite	Phlogotite		2247.36	0.21	2324.14	0.35		-140.08	38581061.82	3319956.82
B21SZK2-33	MgChlorite	Phlogotite		2246.56	0.21	2319.82	0.32	3 data average	-155.57	38581061.82	3319957.28
B21SZK2-36	Montmorillonite	MgChlorite		2241.09	0.08	2318.70	0.19	3 data average	-180.71	38581061.82	3319958.15
B21SZK2-37	MgChlorite			2247.82	0.08	2322.96	0.13		-190.95	38581061.82	3319958.51
B21SZK2-46	Montmorillonite	IntChlorite		2243.88	0.10	2335.21	0.19		-255.00	38581061.82	3319960.74
B21SZK2-47	Montmorillonite	IntChlorite	MgChlorite	2241.85	0.11	2327.52	0.17	3 data average	-256.81	38581061.82	3319960.80
B21SZK2-65	MgChlorite			2248.61	0.03	2326.66	0.06		-354.41	38581061.82	3319965.40
B21SZK2-69	IntChlorite			2259.81	0.08	2341.15	0.08		-369.76	38581061.82	3319966.00
B22SZK1-5	Montmorillonite	MgChlorite		2244.19	0.14	2327.09	0.21		79.77	38580962.33	3319930.99
B22SZK1-15	MgChlorite			2247.97	0.07	2326.51	0.13		-19.32	38580962.34	3319930.23
B22SZK1-24	MgChlorite			2248.89	0.19	2324.07	0.24		-93.02	38580962.46	3319929.55
B22SZK1-52	Montmorillonite	Illite	IntChlorite	2240.55	0.08	2337.99	0.10		-209.27	38580965.07	3319931.54
B22SZK1-62	Calcite	MgChlorite		2252.71	0.06	2324.96	0.06	2 data average	-257.65	38580967.14	3319932.46
B22SZK1-76	Montmorillonite	IntChlorite		2248.23	0.05	2330.71	0.04	2 data average	-317.82	38580968.09	3319934.07
B22SZK1-77	Montmorillonite	MgChlorite		2247.41	0.04	2324.31	0.05	2 data average	-320.41	38580968.12	3319934.15
B22SZK1-79	Montmorillonite	MgChlorite		2248.84	0.05	2324.47	0.07	2 data average	-331.73	38580968.56	3319934.51
B23SZK2-12	Saponite	MgChlorite		2247.81	0.05	2326.28	0.10		-53.61	38580862.07	3319911.30
B23SZK2-23	Montmorillonite	MgChlorite		2245.09	0.29	2326.55	0.38	2 data average	-138.31	38580861.95	3319911.97
B23SZK2-24	Montmorillonite	MgChlorite	Phlogopite	2245.00	0.20	2326.24	0.28		-140.90	38580862.01	3319912.00
B23SZK2-57	IntChlorite			2254.60	0.05	2334.12	0.07	2 data average	-312.67	38580866.51	3319912.79
B23SZK2-64	IntChlorite			2257.28	0.09	2345.97	0.12		-341.26	38580866.76	3319912.81
B23SZK2-65	Calcite	IntChlorite		2260.18	0.05	2339.05	0.06		-343.16	38580866.75	3319912.82
B23SZK2-66	Calcite	MgChlorite	IntChlorite	2251.76	0.04	2331.09	0.07	2 data average	-346.86	38580866.72	3319912.82
B23SZK2-72	Montmorillonite	Illite	IntChlorite	2244.96	0.06	2340.48	0.07	2 data average	-382.46	38580866.42	3319912.90
B23SZK2-73	Montmorillonite	Illite	IntChlorite	2247.33	0.06	2331.42	0.11	2 data average	-399.46	38580866.28	3319912.94
B23SZK2-74	Montmorillonite	MgChlorite		2249.06	0.05	2319.97	0.12	3 data average	-404.86	38580866.24	3319912.96
B23SZK2-75	Montmorillonite	Illite	IntChlorite	2246.21	0.05	2336.67	0.08	2 data average	-410.46	38580866.19	3319912.97
B23SZK2-76	Montmorillonite	MgChlorite	Actinolite	2248.90	0.05	2325.69	0.08	3 data average	-413.06	38580866.17	3319912.97
B23SZK2-77	Montmorillonite	IntChlorite		2252.14	0.09	2335.11	0.13	3 data average	-421.06	38580866.11	3319912.99
B23SZK2-78	Montmorillonite	IntChlorite		2251.95	0.11	2346.22	0.12		-422.46	38580866.09	3319912.99
B23SZK2-79	Montmorillonite	MgChlorite	IntChlorite	2250.43	0.05	2333.32	0.06	2 data average	-365.46	38580866.57	3319912.87
B24SZK1-2	MgChlorite	Saponite		2246.19	0.22	2315.94	0.31		46.16	38580762.75	3319932.78
B24SZK1-3	MgChlorite	Illite		2245.23	0.22	2326.89	0.32		43.56	38580762.74	3319932.78
B24SZK1-4	Montmorillonite	MgChlorite	Dolomite	2245.87	0.19	2323.94	0.31		38.26	38580762.72	3319932.78
B24SZK1-5	Montmorillonite	MgChlorite		2245.74	0.09	2322.61	0.13		35.06	38580762.71	3319932.78
B24SZK1-7	Montmorillonite	Dolomite		2248.20	0.27	2320.11	0.34		29.16	38580762.69	3319932.78
B24SZK1-8	MgChlorite	Phlogopite		2247.03	0.26	2320.34	0.37	3 data average	3.46	38580762.60	3319932.77
B24SZK1-18	MgChlorite	Phlogopite		2246.77	0.29	2315.91	0.40	2 data average	-93.64	38580762.07	3319932.73

5.2. Parameters of chlorite

We have divided the chlorite into three groups according to the reference library of the TSG, i.e., FeChlorite, MgChlorite and IntChlorite (Fig. 7). The SWIR parameters of chlorite for the northern and southern cross sections are presented in Table 1 and 2, separately.

As stated earlier, the key absorption features of chlorite centered around ~2250 nm and ~2350 nm, corresponding to the chlorite FeOH and MgOH bond, respectively (i.e., Pos 2250, Depth 2250, Pos 2350, Dep 2350; Herrmann et al., 2001; Dalton et al., 2014). The Pos 2250 and Pos 2350 values do not show obvious relationships in either cross section, with R^2 values of only 0.013 and 0.150 (Fig. 11a and c), however, the Dep 2250 and Dep 2350 values were strongly coupled, with R^2 values as high as 0.700 and 0.931, respectively (Fig. 11b and d). The Chlorite FeOH absorption features (Pos 2250) were used rather than MgOH (Pos 2350) due to two reasons: 1) the chlorite MgOH absorption features often coincide with the secondary white mica AlOH

features at ca. 2350 nm; 2) Carbonates are abundant in the Tongshankou and they also have overlapping MgOH absorption features in the region of 2350 nm (Herrmann et al., 2001; Dalton et al., 2004; Jones et al., 2005).

In the northern cross section, there are strong spatial relationships between higher Pos 2250 values and the ore bodies in each drillhole (Fig. 12). The Pos 2250 values in drillhole B9WZK2, which is dominated by granodiorite porphyry, range between 2240 and 2251 nm, suggesting a narrow range of the chlorite composition characterized as Mg-rich (Pos 2250 < 2255 nm; Jones et al., 2005). When it comes to the drillholes B9EZK1 and B22NZK2 which contain both porphyry granodiorite, skarn and marble, the value range becomes wider. The Pos 2250 value range is 2242–2260 nm and 2243–2265 nm for B9EZK1 and B22NZK2, respectively, suggesting chlorite compositions ranging from Mg-rich (Pos 2250 < 2255 nm) to Fe-rich (Pos 2250 > 2260 nm; Herrmann et al., 2001; Jones et al., 2005; Huang et al., 2017). No porphyry granodiorite or mineralization were identified in drillhole

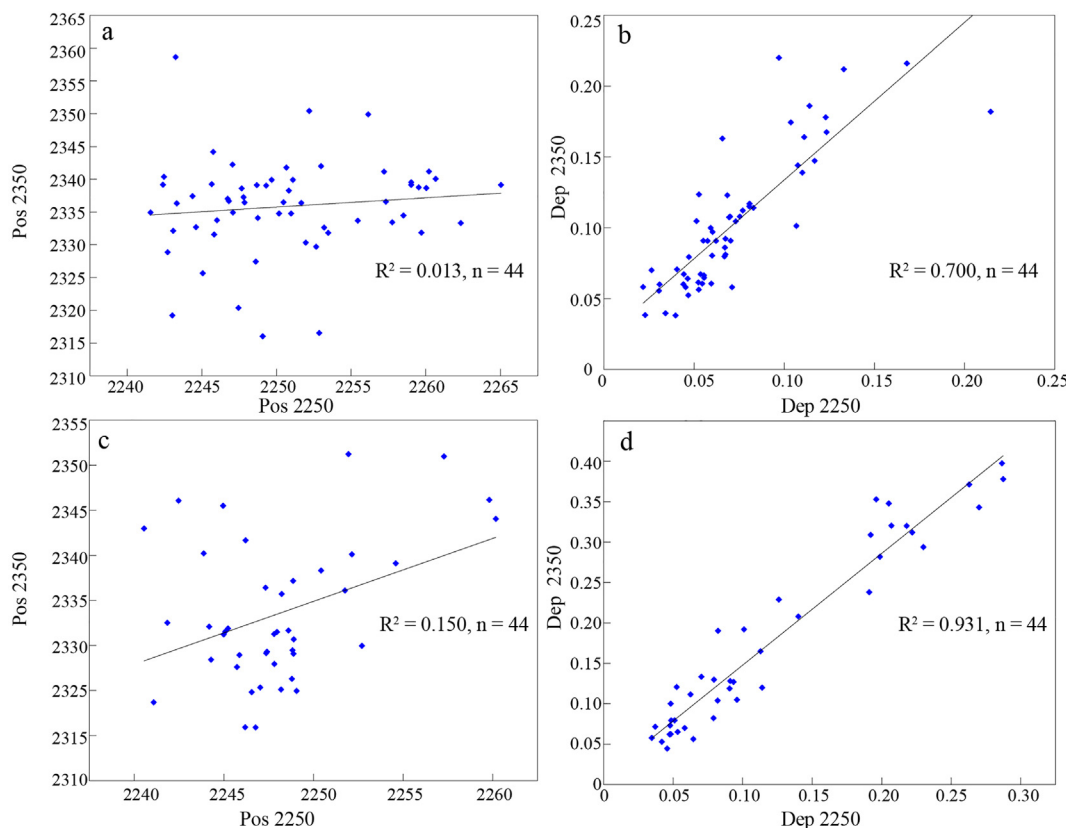


Fig. 11. Plots showing relationship between absorption features of chlorite centered around 2250 and 2350. (a) Pos 2350 vs. Pos 2250 in the northern cross section; (b) Dep 2350 vs. Dep 2250 in the northern cross section; (c) Pos 2350 vs. Pos 2250 in the southern cross section; (d) Dep 2350 vs. Dep 2250 in the southern cross section.

ZK901 and only five samples contained chlorite (Table 1; Fig. 12). The two samples with slightly high Pos 2250 values (higher than 2251 nm) are diorite enclaves, which are unrelated to the mineralization. Similar trends can also be observed in the southern cross section, with the highest Pos 2250 values corresponding well with the position of ore bodies (Fig. 13). But it is difficult to construct a formula to predict distance-to-center using the chlorite Pos 2250 in the Tongshankou mineralization system due to: 1) In the northern cross section, there are several branch ore bodies; 2) In the southern cross section, samples with chlorites are sporadically distributed. However, the positions of ore bodies coincide with high values in the Pos 2250 contour map using the kriging interpolation technique (Fig. 14a and b).

5.3. Chlorite geothermometer

Suitable samples with chlorite from three drillholes B21SZK2, B22SZK1, B23SZK2 in the southern cross section were analysed by EPMA and the results are displayed in Table 3. Chlorite can be a very useful geothermometer based on its non-stoichiometric composition, with the tetrahedral aluminum occupancy and/or the octahedral vacancy as the most important factors during the calculation (Inoue et al., 2009). Sometimes, the calculation of temperatures may need to be calculated using Fe and Mg contents of chlorite: i.e. $T = 106 * Al^{IV} + 0.7 * (Fe/(Fe + Mg)) + 18$ (Kranidiotis and MacLean, 1987), or $T = 319 * (Al^{IV} + (0.1 * Fe/(Fe + Mg))) - 69$ (Jowett, 1991). As no correlation exists between Al^{IV} and $Fe/(Fe + Mg)$ at Tongshankou (Fig. 15a), temperatures of chlorites in this work are based on

$T = -61.92 + 160.99 * Al^{IV}$, which can be generally used in diagenetic, hydrothermal and metamorphic settings (Cathelineau, 1988), without taking Fe and Mg into account. The calculated temperatures at Tongshankou range from 105 to 329 °C. The upper end of the temperature range is consistent with the phyllitic alteration in porphyry mineralization and retrograde alteration in skarn mineralization. The lowest temperature may lead us to take them as diagenetic. But their occurrences as replacement of hornblende, biotite (Fig. 4j and k) and garnet (Fig. 6i) or coexistence with magnetite (Fig. 6m) could imply their hydrothermal origin. Pos 2250 values of chlorite have close negative and positive correlation with the $Mg^#$ and $Fe/(Fe + Mg)$ of chlorite respectively (Fig. 15b and c). However, no correlation existed between calculated temperatures and SWIR parameters (Fig. 15d–f; e.g. Pos 2250, Dep 2250, Pos 2350).

5.4. Parameters of white mica

The SWIR parameters of white mica for the southern cross sections are presented in Table A1. As stated earlier, the most frequently used SWIR parameters for white mica are Pos 2200 and IC (Herrmann et al., 2001; Chang et al., 2011; Yang et al., 2012; Laakso et al., 2016). In the Tongshankou deposit, the Pos 2200 of white mica range from 2198 to 2223 nm, indicating a compositional range from potassic (wavelength between 2200 and 2208 nm) to phengitic muscovite (wavelength > 2216 nm; Table A1; Herrmann et al., 2001; Jones et al., 2005). Unlike in previous studies (Herrmann et al., 2001; Jones et al., 2005; Yang et al., 2012), no relationship exists between the variations of the

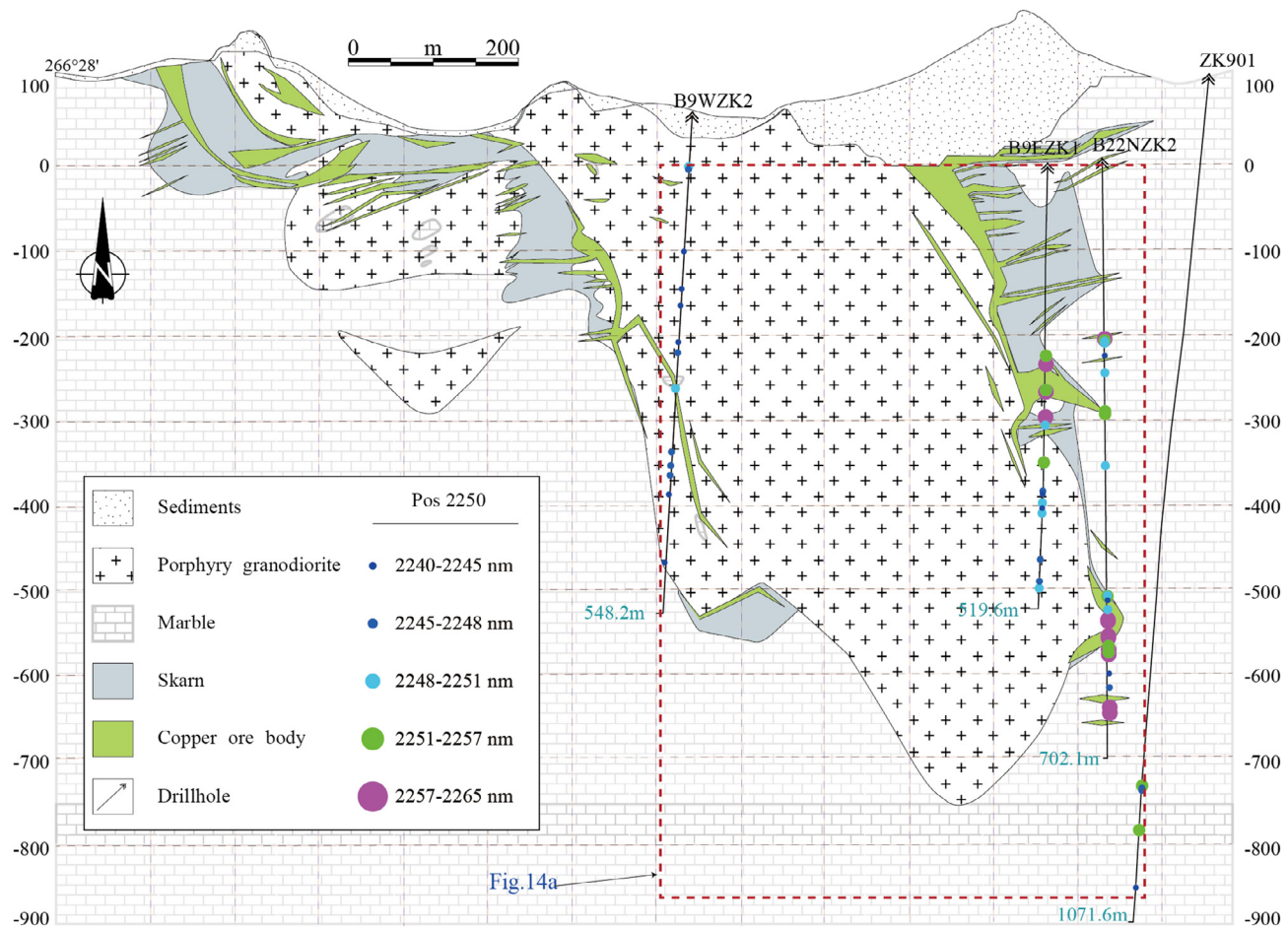


Fig. 12. The distribution of SWIR spectrum parameters for chlorite (Pos 2250) in the northern cross section.

wavelength of Pos 2200 and the distances to the ore bodies at Tongshankou (Supplementary Fig. 1). Similarly, a random distribution of IC values is observed in the cross section (Supplementary Fig. 2).

Supplementary data associated with this article can be found, in the online version, at <https://doi.org/10.1016/j.oregeorev.2018.07.018>.

6. Discussion

6.1. Alteration and mineralization pattern at Tongshankou

At Tongshankou, both porphyry and skarn type mineralization were observed and detailed paragenetic relationships have been reconstructed (Figs. 4–6). The coexistence of porphyry and skarn mineralization is common in many magmatic-hydrothermal systems (Sillitoe, 2010).

Typically, porphyry deposits are characterized by lateral and vertical zones of potassic to propylitic alteration (Sillitoe, 2010; Cooke et al., 2014). Marginal propylitic alteration zones would be detectable kilometres away from the mineralization center such as at the Batu Hijau porphyry deposit (Wilkinson et al., 2015; Neal et al., 2018). The temperature generally decreased gradually from the potassic to

propylitic alteration. At Tongshankou, there is no propylitic alteration. Meanwhile, the Tongshankou stock is only ca. 0.33 km². These means that the alteration zone for the porphyry mineralization was of very limited extent.

Generally, the majority of porphyry deposits worldwide are hosted in volcanic rocks, which are enriched in Fe and Mg (Sillitoe, 2010). Propylitic alteration occurred due to replacement of Fe-Mg-rich minerals such as biotite and hornblende in the volcanic host rocks. However, the host-rocks of the Tongshankou deposit are carbonates which have low Fe, Mg and Al contents. Such Fe-Mg-Al-poor carbonate host-rocks at Tongshankou perhaps explains the absence of the propylitic alteration zone.

6.2. Chlorite SWIR characteristics and ore vectoring

At Tongshankou, the propylitic alteration is not well-developed and consequently, the occurrence of chlorite is mainly linked to the retrograde skarn alteration rather than the porphyry mineralization. Samples with the highest Pos 2250 values are closest to the orebody (Figs. 12–14). Previous studies have shown that good correlations exist between chlorite crystallization temperature and radial distance from

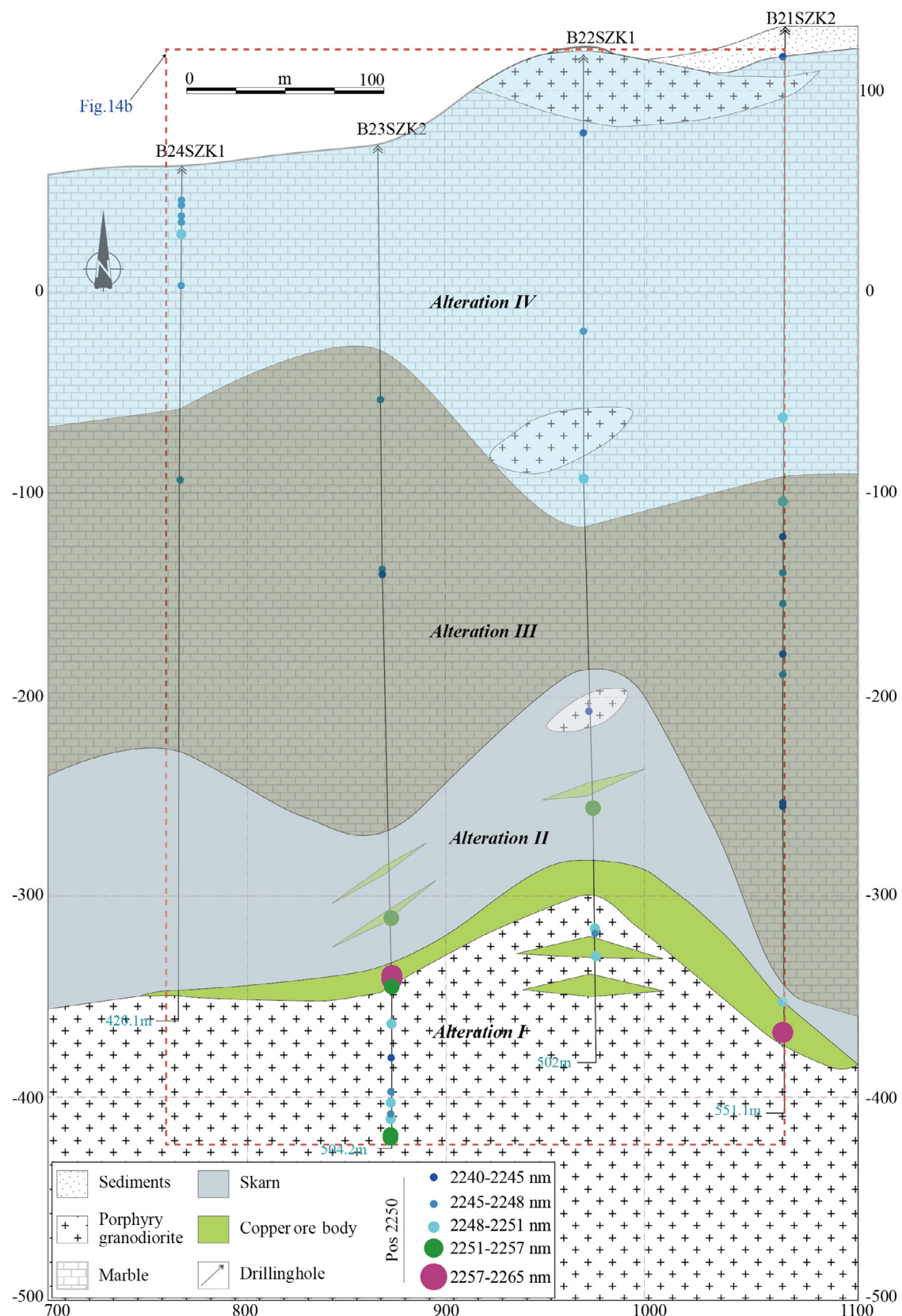


Fig. 13. The distribution of SWIR spectrum parameters for chlorite (Pos 2250) in the southern cross section.

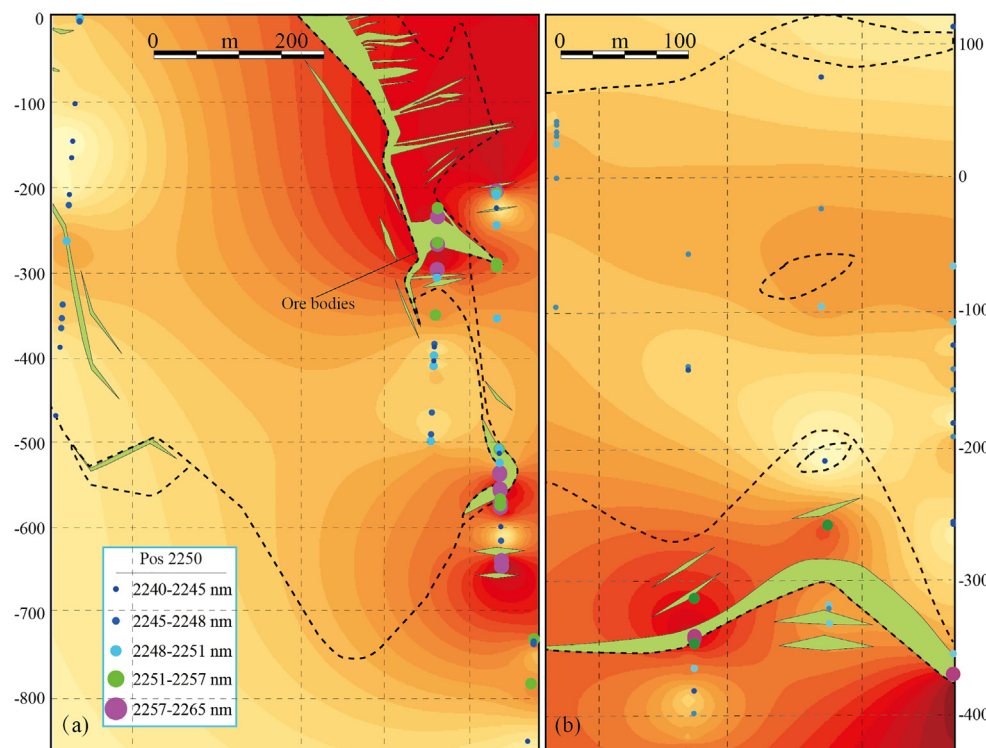


Fig. 14. The ore bodies correlate well with high values in the contour map of Pos 2250 values using the kriging interpolation technique in the northern (a) and southern (b) cross sections. Warmer colours represent higher Pos 2250 values and the green bits on the figures are ore bodies. The black dashed line represent the geological boundary. Fig. a corresponds to the red dashed box in Fig. 12 while Fig. b corresponds to the red dashed box in Fig. 10.

the mineralization center in the Batu Hijau porphyry deposit in Indonesia (Wilkinson et al., 2015). Meanwhile, chlorite Pos 2250 tend to be higher and Fe-rich in the mineralization center at Batu Hijau (Neal et al., 2018). Then Pos 2250 could also reflect the Mg-Fe variations in chlorite at Batu Hijau. The lack of correlation between Al^{IV} and Fe/(Fe + Mg) (Fig. 15a) and Pos 2250 and temperature (Fig. 15d), suggest that temperature may not play any important role to the variations in Pos 2250 values of chlorite at Tongshankou, which is not the same as in Batu Hijau.

Previous studies have shown that the Pos 2250 values of chlorite are positively correlated with the iron content with Fe-rich chlorite always showing a longer wavelength of Pos 2250 than the Mg-rich equivalent (Jones et al., 2005). At Tongshankou, the Pos 2250 values of chlorites show obvious negative correlations with Mg[#] and positive correlations with Fe/(Fe + Mg) (Fig. 15b and c). This suggests the Pos 2250 can be used to reflect the chlorite composition (iron content) at Tongshankou. As Fe-rich chlorite (high Pos 2250) is associated with mineralization, the Pos 2250 can be used as a vector to ore. It is easily to explain that the occurrence of Fe-rich chlorites in the proximity to ore reflects their simultaneous precipitation with magnetite as a result of the late skarn alteration stage fluids. After the precipitation of magnetite, the hydrothermal fluids will be low in iron. When the iron-poor fluids flow through the porphyry granodiorite, they will replace the amphibole and/or biotite (these two minerals are Mg-rich) and form Mg-rich chlorites. Then chlorite can act as an effective potential indicator mineral for exploration in skarn systems.

Although the highest Pos 2250 values of chlorite correlate well with the position of ore bodies in Tongshankou (Figs. 12–14), it is difficult for us to set an effective formula of Pos 2250 with the radial distance from the ore centers in Tongshankou, which may be ascribed to three

reasons: 1) There are many branch ore bodies in the Tongshankou deposit, which will restrict our evaluation of radial distance between the ore bodies and the samples with chlorites, especially in the northern cross section (Fig. 12). 2) Doublier et al. (2010) suggested that SWIR methods are statistical, and the quality and reliability of the data improves with an increasing number of samples. The relatively small number of samples with chlorites at Tongshankou may obscure any clear trend between the radial distance from the ore centers and the SWIR parameters of chlorites. 3) Nearly all the samples in Tongshankou have mixed mineral assemblages. For example, calcites have overlapping absorption features in the region of 2350 nm (Thompson et al., 1999), which may also influence chlorite Pos 2250 and make it difficult to evaluate.

6.3. Implications from SWIR characteristics of white mica

The IC values of white mica have been reported to be positively related to the formation temperatures of the micas and used as exploration tools (Chang and Yang, 2012; Yang et al., 2012). However, the IC distribution pattern of white mica in the Tongshankou deposit shows no strong trends close to the ore (Supplementary Fig. 2). Pos 2200 distribution patterns of white mica also show no regular pattern (Supplementary Fig. 1). Pos 2200 values of white micas shift according to the proportions of octahedral Al and Fe + Mg (Post and Noble, 1993), with high Pos 2200 values corresponding to low ratio of Al^{VI}/(Fe + Mg) (Herrmann et al., 2001; Jones et al., 2005), and thus can act as a monitor of Tschermak exchange ($(\text{Si}^{\text{IV}}(\text{Mg}, \text{Fe})^{\text{VI}} \leftrightarrow \text{Al}^{\text{IV}}\text{Al}^{\text{VI}})$), in which Al^{VI} will increase with high temperature while Mg and Fe will show opposite behaviors (Miyashiro and Shido, 1985; Duke, 1994).

As stated earlier, the Tongshankou deposit lacks the propylitic

Table 3

Composition data of chlorites measured by EPMA and calculated formation temperature.

Spot	SiO ₂	TiO ₂	Al ₂ O ₃	FeO	MnO	MgO	CaO	Na ₂ O	K ₂ O	Cr ₂ O ₃	Total	Si	Al ^{IV}	Al ^{VI}	Fe	Mg	Fe/Fe + Mg	Mg [#]	T (°C)
B21SZK2-65-1	30.24	0.03	15.19	21.38	0.76	18.29	0.11	0.01	0.01	0.06	86.09	6.32	1.68	2.08	3.74	5.7	0.4	0.6	204
B21SZK2-65-2	30.08	0.04	15.07	20.42	0.72	18.72	0.09	0.01	0	0.02	85.17	6.33	1.67	2.08	3.59	5.87	0.38	0.62	203
B21SZK2-65-3	30.62	0.03	15.37	20.54	0.83	19.22	0.11	0	0.01	0	86.72	6.32	1.68	2.07	3.55	5.91	0.37	0.62	204
B21SZK2-69-1	24.67	0.05	19.64	34.78	0.12	5.13	0.25	0	0.07	0.15	84.86	5.65	2.35	2.98	6.66	1.75	0.79	0.21	310
B21SZK2-69-2	25.37	0.07	19.35	35.47	0.03	5.37	0.26	0.02	0.06	0	86	5.73	2.27	2.92	6.7	1.81	0.79	0.21	296
B22SZK1-62-1	29.05	0	17.66	27.21	0	12.31	0.11	0.02	0	0.05	86.41	6.18	1.82	2.64	4.84	3.9	0.55	0.45	223
B22SZK1-62-2	26.94	0.03	18.96	26.82	0	11.64	0.08	0	0.01	0.06	84.53	5.88	2.12	2.79	4.9	3.79	0.56	0.44	273
B22SZK1-62-3	28.89	0.02	17.75	23.69	0.01	14.76	0.08	0	0	0.03	85.23	6.12	1.88	2.59	4.2	4.66	0.47	0.53	233
B22SZK1-76-1	29.56	0.02	16.9	29.68	0.22	11.03	0.12	0.05	0.11	0.22	87.89	6.26	1.74	2.52	5.26	3.48	0.6	0.4	208
B22SZK1-76-2	31.98	0.14	15.61	21.69	0.3	16.79	0.2	0.06	0.8	0.12	87.7	6.51	1.49	2.29	3.69	5.09	0.42	0.58	162
B22SZK1-77-1	24.38	0.04	17.6	21.42	0.19	13.01	0.07	0.11	0.03	0.16	76.99	5.76	2.24	2.7	4.23	4.59	0.48	0.52	292
B22SZK1-77-2	28.35	0.1	17.89	23.53	0.32	15.88	0.01	0.02	0.02	0	86.11	5.98	2.02	2.45	4.15	4.99	0.45	0.55	259
B22SZK1-77-3	27.14	0.01	17.94	26.77	0.29	12.76	0.03	0.01	0.03	0	84.97	5.92	2.08	2.56	4.88	4.15	0.54	0.46	268
B22SZK1-79-1	27.92	0.08	17.67	24.55	0.47	14.87	0.05	0.02	0.03	0.07	85.72	5.96	2.04	2.43	4.39	4.73	0.48	0.52	261
B22SZK1-79-2	28.21	0	17.71	22.56	0.42	15.58	0.04	0	0.01	0.05	84.57	6.03	1.97	2.52	4.03	4.96	0.45	0.55	250
B22SZK1-79-3	27.88	0.04	17.16	24.89	0.49	14.72	0.03	0.01	0.01	0.07	85.3	6	2	2.38	4.48	4.73	0.49	0.51	255
B22SZK1-79-4	27.57	0.04	17.8	24.93	0.43	15.28	0.02	0.03	0.02	0	86.13	5.89	2.11	2.38	4.45	4.86	0.48	0.52	275
B22SZK1-79-5	28.06	0.09	17.76	23.75	0.32	15.61	0.02	0.06	0.02	0.03	85.71	5.96	2.04	2.43	4.22	4.95	0.46	0.54	261
B22SZK1-79-6	27.88	0.05	17.91	24.3	0.38	14.72	0.09	0.04	0.19	0.1	85.66	5.95	2.05	2.48	4.34	4.68	0.48	0.52	261
B23SZK2-57-1	32.48	0.08	13.12	26.75	0.12	15.02	0.27	0.01	0.03	0.06	87.94	6.76	1.24	2	4.65	4.66	0.5	0.5	129
B23SZK2-57-2	32.47	0.02	13.02	24.58	0.21	16.1	0.38	0	0.03	0.12	86.93	6.77	1.23	1.99	4.28	5	0.46	0.54	128
B23SZK2-64-1	28.58	0.04	17.28	31.42	0.52	8	0.24	0.02	0.31	0.09	86.5	6.23	1.77	2.72	5.73	2.6	0.69	0.31	210
B23SZK2-64-2	28.28	0.04	18.17	32.17	0.53	8.06	0.35	0.01	0.18	0.09	87.88	6.09	1.91	2.75	5.8	2.59	0.69	0.31	235
B23SZK2-64-3	26.37	0.05	17.46	33.32	0.57	7.13	0.5	0.04	0.07	0.58	86.08	5.92	2.08	2.57	6.25	2.39	0.72	0.28	266
B23SZK2-65-1	25.95	0.02	15.08	37.79	0.61	5.88	0.2	0.14	0.03	0.2	85.9	6.03	1.97	2.18	7.35	2.04	0.78	0.22	251
B23SZK2-65-2	26.19	0.02	14.51	38.93	0.63	5.59	0.22	0.04	0	0.08	86.2	6.1	1.9	2.1	7.59	1.94	0.8	0.2	241
B23SZK2-65-3	25.09	0.02	15.01	35.61	0.69	6.08	0.24	0.03	0.01	0.04	82.81	6.01	1.99	2.26	7.14	2.17	0.77	0.23	255
B23SZK2-73-1	31.98	0.02	13.81	22.6	0.05	17.54	0.27	0.03	0.01	0	86.3	6.64	1.36	2.05	3.93	5.43	0.42	0.58	148
B23SZK2-73-2	31.53	0	15.62	18.72	0.15	20.87	0.16	0.01	0.02	0.03	87.09	6.38	1.62	2.12	3.17	6.29	0.33	0.66	194
B23SZK2-73-3	31.88	0.09	14.7	18.82	0.14	20.51	0.11	0.02	0.01	0.03	86.31	6.5	1.5	2.05	3.21	6.23	0.34	0.66	173
B23SZK2-74-1	31.93	0.03	15.36	17.77	0.21	20.25	0.37	0.04	0.17	0.72	86.83	6.44	1.56	2.13	3	6.09	0.33	0.67	179
B23SZK2-75-1	28.97	0.05	15.89	27.25	0.26	14.02	0.18	0	0.07	0.09	86.78	6.19	1.81	2.22	4.87	4.47	0.52	0.48	224
B23SZK2-75-2	27.82	0.15	17.86	20.95	0.13	18.68	0.05	0	0.08	0.23	85.94	5.83	2.17	2.25	3.67	5.84	0.39	0.61	285
B23SZK2-76-1	25.86	0	18.54	22.45	0.31	17.48	0.05	0	0	0	84.69	5.57	2.43	2.29	4.1	5.62	0.42	0.58	329
B23SZK2-76-2	28.1	0.05	18.11	22.34	0.35	17.39	0.07	0	0.03	0.05	86.48	5.88	2.12	2.37	3.91	5.43	0.42	0.58	276
B23SZK2-76-3	28.49	0	17.7	22.88	0.29	16.95	0.07	0.01	0.01	0.01	86.43	5.97	2.03	2.37	4.01	5.3	0.43	0.57	260
B23SZK2-76-4	27.89	0.03	18.74	23.91	0.34	16.28	0.02	0.01	0	0.03	87.26	5.83	2.17	2.46	4.18	5.07	0.45	0.55	285
B23SZK2-77-1	31.23	0.05	13.09	28.65	0.07	12.76	0.35	0.03	0.05	0.16	86.44	6.71	1.29	2.05	5.14	4.08	0.56	0.44	137
B23SZK2-77-2	31.43	0.03	13.97	29.19	0.11	11.96	0.32	0.01	0.09	0.18	87.29	6.68	1.32	2.21	5.18	3.79	0.58	0.42	140
B23SZK2-77-3	32.34	0	13.05	28.53	0.05	13.1	0.34	0.04	0.03	0.06	87.54	6.81	1.19	2.08	5.03	4.11	0.55	0.45	118
B23SZK2-77-4	32.67	0.02	12.45	28.31	0.09	13.06	0.36	0.06	0.04	0.32	87.38	6.89	1.11	2.02	4.99	4.11	0.55	0.45	105
B23SZK2-78-1	27.86	0.06	17.39	33.94	0.06	6.48	0.3	0.01	0.11	0.02	86.23	6.18	1.82	2.76	6.29	2.14	0.75	0.25	221
B23SZK2-78-2	28.6	0.08	18.34	31.54	0.07	6.24	0.1	0	0.4	0.07	85.44	6.27	1.73	3.07	5.78	2.04	0.74	0.26	200
B23SZK2-78-3	24.84	0.08	18.61	34.82	0.07	6.67	0.06	0	0.06	0.1	85.31	5.67	2.33	2.71	6.65	2.27	0.75	0.25	308

alteration zone found in many porphyry deposits due to their Fe-Mg-Al poor carbonate host-rocks. These host-rocks not only restrict the development of a propylitic alteration zone but also prevent Tschermark exchange in white mica ($(\text{Si}^{\text{IV}}(\text{Mg}, \text{Fe})^{\text{VI}} \leftrightarrow \text{Al}^{\text{IV}}\text{Al}^{\text{VI}})$), which may in turn obscure any trend of SWIR parameters of white mica such as Pos 2250 and IC. Meanwhile, the small volume of the Tongshankou stock (ca. 0.33 km³) limits the alteration zone for the porphyry mineralization, which may further obscure the trend of Pos 2250 and IC of white mica. Thus, the SWIR spectroscopy of white mica should be used cautiously during exploration in the Tongshankou deposit and other porphyry-skarn deposits whose host rocks are mainly carbonates.

7. Conclusions

Alteration of the Tongshankou Cu-Mo deposit could be divided into porphyry type and skarn type. Alteration in the porphyry mineralization consists of potassic alteration, phyllitic alteration and a carbonate stage. The main porphyry mineralization is associated with phyllitic

alteration. No propylitic alteration is present at Tongshankou. The skarn-type alteration comprises early skarn stage, late skarn stage, oxide stage, quartz-sulfide stage and late vein stage. The quartz-sulfide stage hosts the majority of mineralization in the Tongshankou deposit. At Tongshankou, the propylitic alteration is not well-developed and the occurrence of chlorite is mainly linked to the retrograde skarn alteration rather than the porphyry mineralization. Based on SWIR data, white mica trends do not work well as a vector to mineralization or a proxy for alteration in the Tongshankou deposit, likely due to the carbonate host rocks. Combined with SWIR and EPMA data, chlorite crystallization temperatures do not change systematically with the distances to ore. However, chlorites proximal to the ore bodies are Fe-rich and have high Pos 2250 (> 2251 nm) while distal chlorites tend to be Mg-rich and have low Pos 2250. Then SWIR spectroscopy of chlorite may not only be an applicable exploration tool in the Tongshankou deposit but also has potential to be used in other intrusion-related skarn hydrothermal system.

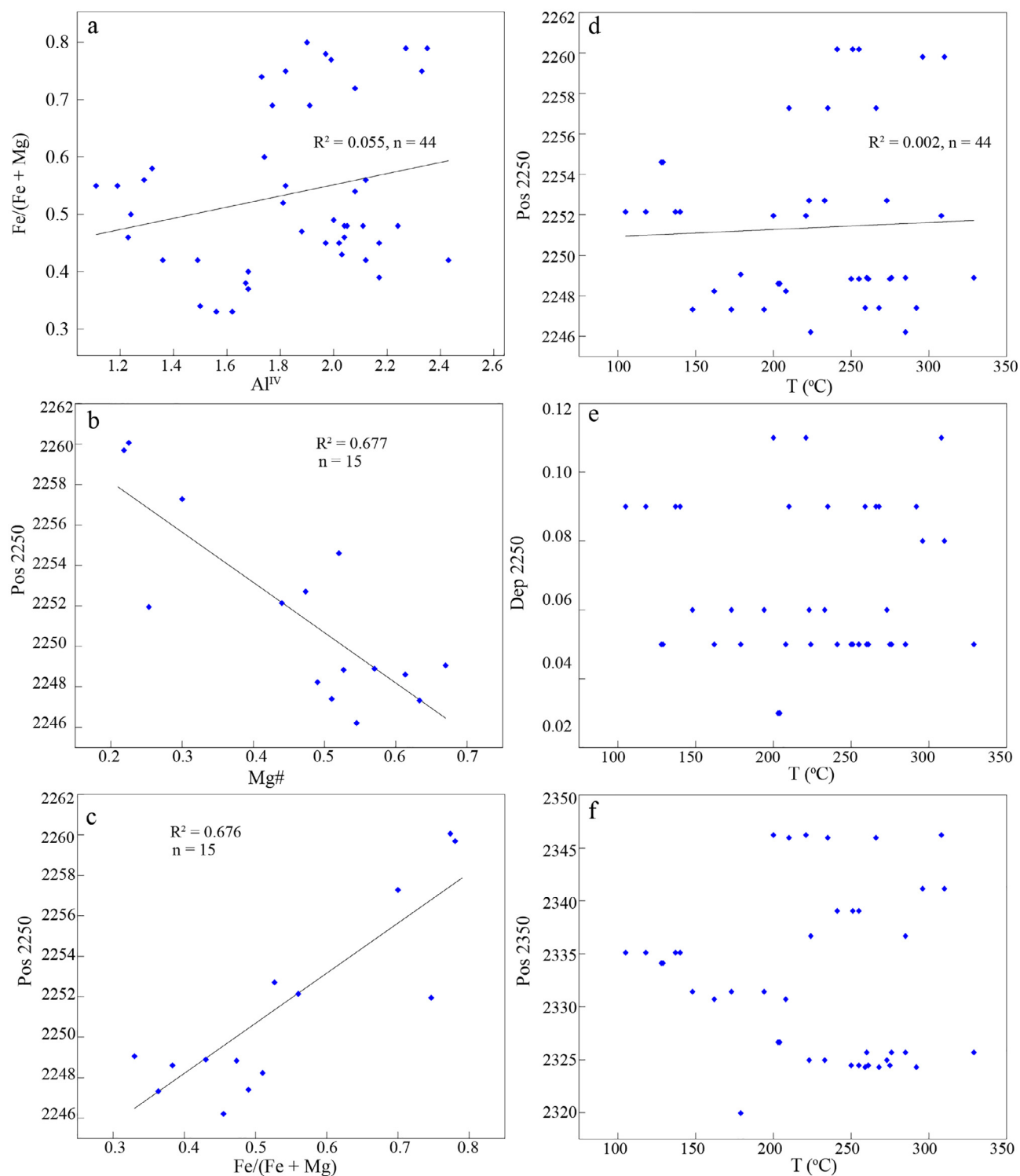


Fig. 15. Plots showing relationship between (a) Al^{IV} vs. $\text{Fe}/(\text{Fe} + \text{Mg})$ in the chlorites; (b) $\text{Pos}\ 2250$ vs. the formation temperature of the chlorites; (c) average $\text{Pos}\ 2250$ vs. average $\text{Mg}^\#$ ($\text{Mg}/(\text{Mg} + \text{Fe})$) in the chlorites; (d) average $\text{Pos}\ 2250$ vs. average $\text{Fe}/(\text{Fe} + \text{Mg})$.

Acknowledgements

This study was funded by the National Natural Science Foundation of China (NSFC Grant 41502065), the Special Public Welfare Scientific Research fund Project by Ministry of Land and Resources, China (201511035), CAS Creative and Interdisciplinary Program

(Y433131A07) and the China Scholarship Council. We would like to thank Xiaobo Zhang and Zeming Li for their help during field work. We are grateful to the two anonymous reviewers for their constructive comments, and David Lentz for handling the manuscript. This is contribution No. IS-2563 from GIGCAS.

Appendix

See Table A1

Table A1

SWIR results of white mica in the southern cross section of the Tongshankou deposit.

Sample	Mineral 1	Mineral 2	Mineral 3	Pos1900	Dep1900	Pos2200	Dep2200	IC	Remarks	Depth	x	y
B21SZK2-3	Montmorillonite	Illite	IntChlorite	1912.89	0.26	2212.22	0.10	0.39	3 data average	117.81	38581061.82	3319951.32
B21SZK2-4	Montmorillonite	Illite		1911.56	0.27	2209.02	0.12	0.44	3 data average	110.75	38581061.82	3319951.44
B21SZK2-5	Illite			1911.16	0.30	2207.59	0.33	1.11	3 data average	94.06	38581061.82	3319951.73
B21SZK2-6	Illite			1910.59	0.31	2209.19	0.36	1.15	2 data average	84.70	38581061.82	3319951.90
B21SZK2-7	Illite			1910.30	0.38	2204.14	0.42	1.14	3 data average	78.66	38581061.82	3319952.00
B21SZK2-8	Montmorillonite	Illite		1911.33	0.37	2203.21	0.39	1.04	3 data average	74.06	38581061.82	3319952.08
B21SZK2-9	Montmorillonite	Illite		1911.35	0.45	2202.02	0.46	1.02	3 data average	71.52	38581061.82	3319952.13
B21SZK2-11	Illite			1912.55	0.13	2202.20	0.17	1.30	3 data average	61.56	38581061.82	3319952.30
B21SZK2-16	Montmorillonite	Calcite		1923.10	0.09	2207.78	0.08	0.92		16.97	38581061.82	3319953.08
B21SZK2-17	Montmorillonite	Illite	Calcite	1914.53	0.17	2206.72	0.09	0.57	3 data average	12.92	38581061.82	3319953.15
B21SZK2-24	Montmorillonite	Calcite		1911.15	0.24	2210.32	0.12	0.48		-59.72	38581061.82	3319954.45
B21SZK2-27	Montmorillonite	Calcite		1912.33	0.27	2211.22	0.09	0.36	2 data average	-76.91	38581061.82	3319954.96
B21SZK2-28	Montmorillonite	Calcite	Ankerite	1912.29	0.18	2219.14	0.09	0.51	3 data average	-91.23	38581061.82	3319955.39
B21SZK2-29	Montmorillonite	MgChlorite		1911.08	0.45	2203.78	0.22	0.49		-104.60	38581061.82	3319955.79
B21SZK2-31	Montmorillonite	MgChlorite		1912.18	0.38	2201.73	0.20	0.51		-122.09	38581061.82	3319956.30
B21SZK2-35	Montmorillonite	Dolomite		1911.58	0.18	2217.20	0.09	0.49		-174.66	38581061.82	3319957.96
B21SZK2-36	Montmorillonite	MgChlorite		1911.64	0.34	2209.13	0.10	0.29	3 data average	-180.71	38581061.82	3319958.17
B21SZK2-40	Montmorillonite	Dolomite		1918.00	0.07	2208.79	0.07	1.06		-215.64	38581061.82	3319959.39
B21SZK2-43	Montmorillonite	Dolomite	Calcite	1914.39	0.11	2208.41	0.08	0.74	3 data average	-235.52	38581061.82	3319960.08
B21SZK2-45	Montmorillonite	Illite	Phlogopite	1911.01	0.18	2209.80	0.15	0.82	3 data average	-252.91	38581061.82	3319960.69
B21SZK2-46	Montmorillonite	MgChlorite	Dolomite	1911.14	0.16	2217.74	0.08	0.53	2 data average	-255.00	38581061.82	3319960.76
B21SZK2-47	Montmorillonite	MgChlorite	IntChlorite	1911.64	0.25	2214.24	0.13	0.70	3 data average	-256.81	38581061.82	3319960.83
B21SZK2-68	Montmorillonite	Illite		1907.98	0.11	2210.47	0.10	0.85		-366.14	38581061.82	3319965.90
B21SZK2-70	Montmorillonite	Illite		1916.27	0.31	2205.42	0.17	0.53	3 data average	-373.70	38581061.82	3319966.19
B21SZK2-71	Montmorillonite	Illite		1912.11	0.36	2203.50	0.33	0.91	3 data average	-378.05	38581061.82	3319966.36
B21SZK2-72	Montmorillonite	Illite		1917.84	0.32	2201.59	0.14	0.46	3 data average	-392.22	38581061.82	3319966.90
B21SZK2-73	Montmorillonite	Illite		1916.31	0.29	2202.73	0.12	0.42	3 data average	-393.12	38581061.82	3319966.94
B21SZK2-74	Montmorillonite	Illite		1909.88	0.17	2211.76	0.12	0.78	3 data average	-407.56	38581061.82	3319967.49
B22SZK1-2	Illite			1911.22	0.26	2209.90	0.34	1.31	2 data average	85.47	38580962.32	3319931.02
B22SZK1-3	Illite			1909.69	0.20	2211.18	0.30	1.51	2 data average	84.97	38580962.32	3319931.01
B22SZK1-5	Montmorillonite	Illite	MgChlorite	1914.08	0.13	2213.04	0.16	1.31	2 data average	79.77	38580962.33	3319930.99
B22SZK1-6	Montmorillonite	Calcite		1912.27	0.17	2216.51	0.08	0.52	2 data average	77.57	38580962.33	3319930.98
B22SZK1-8	Montmorillonite	Calcite		1918.57	0.14	2208.98	0.08	0.56	2 data average	31.37	38580962.36	3319930.74
B22SZK1-11	Montmorillonite	Calcite		1918.00	0.10	2213.99	0.06	0.56	2 data average	2.17	38580962.36	3319930.48
B22SZK1-12	Montmorillonite	Calcite		1919.30	0.10	2210.56	0.06	0.57		0.77	38580962.36	3319930.46
B22SZK1-14	Montmorillonite	Illite	Halloysite	1913.12	0.16	2208.01	0.16	1.04	2 data average	-15.63	38580962.35	3319930.26
B22SZK1-15	Montmorillonite	MgChlorite	Calcite	1911.46	0.30	2209.02	0.12	0.42	2 data average	-19.32	38580962.34	3319930.22
B22SZK1-16	Montmorillonite	Illite	Halloysite	1910.90	0.34	2209.00	0.21	0.62	3 data average	-34.92	38580962.33	3319930.03
B22SZK1-17	Montmorillonite	Calcite		1924.49	0.20	2208.25	0.11	0.54		-52.12	38580962.32	3319929.82
B22SZK1-18	Montmorillonite	Illite	Calcite	1911.39	0.24	2209.84	0.16	0.65	2 data average	-59.82	38580962.31	3319929.73
B22SZK1-19	Montmorillonite	Halloysite		1910.70	0.34	2208.27	0.34	1.00	3 data average	-60.52	38580962.31	3319929.72
B22SZK1-20	Montmorillonite	Illite	Dolomite	1912.22	0.32	2207.65	0.24	0.72	2 data average	-68.52	38580962.30	3319929.62
B22SZK1-21	Montmorillonite	Dolomite	Calcite	1911.67	0.15	2216.71	0.09	0.64	3 data average	-70.92	38580962.30	3319929.59
B22SZK1-23	Montmorillonite	Illite		1911.20	0.37	2219.14	0.22	0.60		-90.12	38580962.39	3319929.49
B22SZK1-25	Montmorillonite	Dolomite		1912.34	0.12	2222.44	0.08	0.70	2 data average	-98.62	38580962.58	3319929.62
B22SZK1-26	Montmorillonite	Dolomite		1912.33	0.14	2221.41	0.09	0.70	2 data average	-102.91	38580962.67	3319929.69
B22SZK1-28	Montmorillonite	Illite		1911.40	0.21	2210.06	0.10	0.47	2 data average	-109.71	38580962.81	3319929.79
B22SZK1-29	Montmorillonite	Illite	Calcite	1912.43	0.14	2214.49	0.08	0.54	2 data average	-114.71	38580962.92	3319929.87
B22SZK1-31	Illite			1911.00	0.25	2210.66	0.32	1.29	3 data average	-122.11	38580963.08	3319929.98
B22SZK1-42	Montmorillonite	Calcite		1920.79	0.19	2208.72	0.07	0.44	2 data average	-163.39	38580963.96	3319930.60
B22SZK1-43	Montmorillonite	Dolomite		1923.36	0.06	2209.67	0.07	1.33		-165.89	38580964.01	3319930.64
B22SZK1-47	Montmorillonite	Calcite		1915.94	0.15	2204.39	0.06	0.42		-201.48	38580964.86	3319931.21
B22SZK1-48	Illite	Calcite		1916.91	0.13	2205.51	0.12	0.89	3 data average	-203.18	38580964.91	3319931.24
B22SZK1-49	Illite			1912.50	0.26	2200.00	0.22	0.89	3 data average	-203.88	38580964.92	3319931.26
B22SZK1-51	Montmorillonite	Illite		1914.87	0.09	2199.41	0.08	0.84		-207.27	38580965.01	3319931.31
B22SZK1-52	Illite			1911.95	0.37	2201.92	0.33	0.87	3 data average	-209.27	38580965.07	3319931.35
B22SZK1-53	Illite			1912.20	0.42	2197.84	0.33	0.79	3 data average	-211.27	38580965.12	3319931.38
B22SZK1-54	Illite			1911.95	0.27	2200.01	0.22	0.83	3 data average	-213.17	38580965.17	3319931.42
B22SZK1-55	Montmorillonite	Illite		1915.24	0.36	2204.04	0.21	0.56	3 data average	-235.36	38580965.75	3319931.80
B22SZK1-69	Montmorillonite	Illite		1909.60	0.37	2209.42	0.31	0.83	2 data average	-295.63	38580967.43	3319933.01
B22SZK1-70	Montmorillonite	Illite		1910.88	0.23	2210.33	0.19	0.85	3 data average	-301.53	38580967.50	3319933.20
B22SZK1-71	Montmorillonite	Illite		1909.64	0.19	2209.96	0.19	1.02	3 data average	-303.62	38580967.55	3319933.26
B22SZK1-72	Montmorillonite	Illite		1911.29	0.23	2209.65	0.18	0.76	3 data average	-305.82	38580967.59	3319933.33
B22SZK1-73	Montmorillonite	Illite		1910.46	0.33	2208.59	0.27	0.82	3 data average	-308.02	38580967.72	3319933.40
B22SZK1-74	Montmorillonite	Illite		1914.13	0.29	2206.27	0.13	0.48	3 data average	-310.42	38580967.77	3319933.47
B22SZK1-75	Montmorillonite	Illite		1914.59	0.17	2209.78	0.11	0.62	3 data average	-314.92	38580967.93	3319933.61
B22SZK1-76	Montmorillonite	IntChlorite		1915.56	0.08	2214.65	0.05	0.57	2 data average	-317.82	38580968.09	3319933.71
B22SZK1-77	Montmorillonite	MgChlorite		1912.30	0.10	2206.55	0.05	0.49	2 data average	-320.41	38580968.12	3319933.79
B22SZK1-78	Montmorillonite	Illite		1910.83	0.26	2210.70	0.19	0.75	2 data average	-328.33	38580968.25	3319934.03

(continued on next page)

Table A1 (continued)

Sample	Mineral 1	Mineral 2	Mineral 3	Pos1900	Dep1900	Pos2200	Dep2200	IC	Remarks	Depth	x	y
B22SZK1-79	Montmorillonite	MgChlorite		1913.18	0.06	2207.27	0.04	0.59		-331.73	38580968.56	3319934.14
B23SZK2-2	Montmorillonite	Muscovite	Calcite	1915.88	0.10	2210.41	0.12	1.38	3 data average	39.98	38580862.62	3319910.48
B23SZK2-3	Montmorillonite	Calcite		1920.01	0.10	2208.46	0.08	0.79	2 data average	27.48	38580862.53	3319910.61
B23SZK2-4	Montmorillonite	Calcite		1916.01	0.07	2208.41	0.08	1.22	2 data average	10.09	38580862.42	3319910.78
B23SZK2-5	Montmorillonite	Dolomite		1924.64	0.23	2208.82	0.09	0.40		5.79	38580862.39	3319910.83
B23SZK2-6	Montmorillonite	Dolomite		1915.57	0.16	2208.21	0.15	0.98		2.89	38580862.37	3319910.86
B23SZK2-8	Montmorillonite	Calcite		1918.02	0.20	2220.86	0.08	0.43	2 data average	-16.91	38580862.23	3319911.06
B23SZK2-10	Montmorillonite	Dolomite		1918.54	0.12	2208.09	0.10	0.86	2 data average	-30.11	38580862.16	3319911.18
B23SZK2-23	Montmorillonite	MgChlorite		1913.73	0.45	2205.51	0.35	0.78		-138.31	38580861.95	3319912.04
B23SZK2-24	Montmorillonite	MgChlorite		1911.58	0.24	2209.11	0.13	0.53	2 data average	-140.90	38580862.01	3319912.07
B23SZK2-36	Montmorillonite	Calcite		1914.90	0.10	2222.54	0.05	0.46		-209.16	38580863.55	3319912.71
B23SZK2-54	Montmorillonite	Illite		1910.04	0.28	2217.68	0.20	0.72		-302.04	38580866.19	3319912.58
B23SZK2-55	Montmorillonite	Calcite		1916.72	0.14	2208.40	0.07	0.52	3 data average	-303.67	38580866.24	3319912.57
B23SZK2-56	Montmorillonite	Calcite		1908.81	0.40	2215.78	0.18	0.45		-304.47	38580866.26	3319912.57
B23SZK2-58	Montmorillonite	Illite	Calcite	1911.57	0.15	2208.71	0.10	0.68	3 data average	-314.87	38580866.57	3319912.54
B23SZK2-68	Montmorillonite	Illite		1912.31	0.31	2204.95	0.22	0.92	3 data average	-352.66	38580866.67	3319912.58
B23SZK2-69	Montmorillonite	Illite		1913.75	0.36	2205.01	0.20	0.54	3 data average	-359.18	38580866.62	3319912.60
B23SZK2-70	Montmorillonite	Illite		1911.84	0.27	2206.86	0.18	0.67	3 data average	-366.26	38580866.56	3319912.62
B23SZK2-71	Montmorillonite	Illite	Dolomite	1913.73	0.28	2203.65	0.18	0.77	3 data average	-369.76	38580866.53	3319912.63
B23SZK2-72	Montmorillonite	Illite	IntChlorite	1911.41	0.17	2209.10	0.11	0.64	3 data average	-382.46	38580866.42	3319912.66
B23SZK2-73	Montmorillonite	Illite	IntChlorite	1918.69	0.27	2200.86	0.10	0.40	3 data average	-399.46	38580866.28	3319912.71
B23SZK2-74	Montmorillonite	Phlogopite	Actinolite	1914.73	0.07	2205.95	0.05	0.80	3 data average	-404.86	38580866.24	3319912.73
B23SZK2-75	Montmorillonite	Illite	IntChlorite	1919.61	0.18	2203.29	0.06	0.37	2 data average	-410.46	38580866.19	3319912.74
B23SZK2-76	Montmorillonite	MgChlorite	Actinolite	1917.69	0.06	2206.68	0.04	0.71		-413.06	38580866.17	3319912.75
B23SZK2-77	Montmorillonite	IntChlorite		1912.49	0.11	2218.41	0.06	0.53		-421.06	38580866.11	3319912.77
B23SZK2-78	Montmorillonite	IntChlorite	Calcite	1914.41	0.10	2210.42	0.10	1.50	3 data average	-422.46	38580866.09	3319912.78
B23SZK2-79	Montmorillonite	Illite	IntChlorite	1912.70	0.11	2209.33	0.09	0.79	3 data average	-365.46	38580866.57	3319912.61
B23SZK2-13	Montmorillonite	Dolomite		1910.72	0.23	2211.69	0.14	0.63		-70.94	38580862.00	3319932.78
B24SZK1-2	Montmorillonite	Phlogopite		1912.12	0.19	2208.70	0.09	0.46		46.16	38580762.75	3319932.78
B24SZK1-3	Montmorillonite	MgChlorite	Dolomite	1912.57	0.31	2210.25	0.18	0.59	2 data average	43.56	38580762.74	3319932.78
B24SZK1-4	Montmorillonite	Dolomite		1912.19	0.20	2220.28	0.14	0.72	3 data average	38.26	38580762.72	3319932.78
B24SZK1-7	Illite			1912.28	0.38	2202.24	0.49	1.31		29.16	38580762.69	3319932.77
B24SZK1-10	Montmorillonite	Dolomite		1911.67	0.34	2219.63	0.19	0.56		-6.34	38580762.57	3319932.77
B24SZK1-11	Montmorillonite	Dolomite		1920.66	0.11	2221.83	0.05	0.51		-11.84	38580762.55	3319932.76
B24SZK1-12	Montmorillonite	Dolomite		1918.01	0.18	2210.55	0.12	0.71	3 data average	-44.04	38580762.42	3319932.75
B24SZK1-13	Montmorillonite	Calcite		1911.60	0.28	2215.57	0.12	0.42		-57.24	38580762.33	3319932.58
B24SZK1-42	Illite			1924.96	0.24	2202.26	0.04	0.18		-342.34	38580759.78	3319932.57
B24SZK1-43	Montmorillonite	Illite		1913.98	0.31	2205.66	0.19	0.61	3 data average	-342.84	38580759.78	3319932.57
B24SZK1-44	Montmorillonite	Illite		1912.57	0.38	2205.69	0.23	0.61	3 data average	-344.64	38580759.75	3319932.57
B24SZK1-45	Montmorillonite	Calcite		1915.23	0.10	2212.97	0.07	0.74	3 data average	-347.44	38580759.71	3319932.57
B24SZK1-46	Montmorillonite	Illite		1918.84	0.29	2201.90	0.12	0.40	3 data average	-351.44	38580759.66	3319932.56
B24SZK1-47	Montmorillonite	Illite		1921.10	0.21	2207.14	0.06	0.29	2 data average	-354.04	38580759.62	3319932.57
B24SZK1-48	Montmorillonite	Illite		1915.17	0.32	2202.72	0.19	0.58	3 data average	-352.14	38580759.65	3319932.56
B24SZK1-49	Montmorillonite	Illite		1916.76	0.42	2200.85	0.27	0.62	3 data average	-358.14	38580759.56	38580759.56

References

- Cathelineau, M., 1988. Cation site occupancy in chlorites and illites as function of temperature. *Clay Miner.* 23, 471–485.
- Chang, Y.F., Liu, X.P., Wu, Y.C., 1991. The copper-iron belt of the lower and middle reaches of the Changjiang River. Geological Publishing House, Beijing, pp. 379 in Chinese with English abstract.
- Chang, Z.S., Hedenquist, J.W., White, N.C., Cooker, D.R., Roach, M., Deyell, C.L., Garcia, J., Gemmell, J.B., McKnight, S., Cuson, A.L., 2011. Exploration tools for linked porphyry and epithermal deposits: example from the Mankayan intrusion-centered Cu-Au District, Luzon, Philippines. *Econ. Geol.* 106, 1365–1398.
- Chang, Z.S., Yang, Z.M., 2012. Evaluation of inter-instrument variations among short wavelength infrared (SWIR) devices. *Econ. Geol.* 107, 1479–1488.
- R. Clark, G. Swazey, R. Wise, E. Livo, T. Hoefen, R. Kokaly, S. Sutley, 2007. USGS spectral library split06a U.S. Geological Survey, Digital Data Series 321, Online Available at: <<http://speclab.cr.usgs.gov/spectral-lib.html>> (accessed 14).
- Cooke, D.R., Hollings, P., Wilkinson, J.J., Tosdal, R.M., 2014. Geochemistry of porphyry deposits. In: Turekian, H.D., Holland, K.K. (Eds.), *Treatise on Geochemistry*, Second ed. Elsevier, Oxford, pp. 357–381.
- Dalm, M., Buxton, M.W., van Ruitenbeek, Frank J.A., Voncken, J.H., 2014. Application of near-infrared spectroscopy to sensor based sorting of a porphyry copper ore. *Miner. Eng.* 58, 7–16.
- Dalm, M., Buxton, M., van Ruitenbeek, F., 2017. Discriminating ore and waste in a porphyry copper deposit using short-wavelength infrared (SWIR) hyperspectral imagery. *Miner. Eng.* 105, 10–18.
- Dalton, J.B., Bove, D.J., Mladinich, C.S., Rockwell, B.W., 2004. Identification of spectrally similar materials using the USGS Tetraorder algorithm: the calcite–epidote–chlorite problem. *Remote Sens. Environ.* 89, 455–466.
- Doublier, M.P., Roache, T., Potel, S., 2010. Short-wavelength infrared spectroscopy: a new petrological tool in low-grade to very low-grade pelites. *Geology* 38, 1031–1034.
- Duke, E.F., 1994. Near infrared spectra of muscovite, Tschermark substitution, and metamorphic reaction progress: implications for remote sensing. *Geology* 22, 621–624.
- Harraden, C.L., McNulty, B.A., Gregory, M.J., Lang, J.R., 2013. Shortwave infrared spectral analysis of hydrothermal alteration associated with the pebble porphyry copper-gold-molybdenum deposit, Iliamna, Alaska. *Econ. Geol.* 108, 483–494.
- Herrmann, W., Blake, M., Doyle, M., Huston, D., Kamprad, J., Merry, N., Pontual, S., 2001. Short wavelength infrared (SWIR) spectral analysis of hydrothermal alteration zones associated with base metal sulfide deposits at Rosebery and Western Tharsis, Tasmania, and Highway-Reward, Queensland. *Econ. Geol.* 96, 939–955.
- Huang, J.H., Chen, H.Y., Han, J.S., Deng, X.H., Lu, W.J., Zhu, R.L., 2017. Alteration zoning and short wavelength infrared (SWIR) characteristics of the Honghai VMS Cu-Zn deposit, Eastern Tianshan, NW China. *Ore Geol. Rev.* <https://doi.org/10.1016/j.oregeorev.2017.02.037>.
- Hunt, G., 1979. Spectral signatures of particulate minerals in the visible and near infrared. *Geophysics* 42, 501–503.
- Inoue, A., Meunier, A., Patrier-Mas, P., Rigault, C., Beaufort, D., Viellard, P., 2009. Application of chemical geothermometry to low-temperature trioctahedral chlorites. *Clays Clay Miner.* 57, 371–382.
- Jones, S., Herrmann, W., Gemmell, J.B., 2005. Short Wavelength Infrared Spectral Characteristics of the HW horizon: implications for exploration in the Myra Falls volcanic-hosted massive sulfide camp, Vancouver Island, British Columbia, Canada. *Econ. Geol.* 100, 273–294.
- Jowett, E.C., 1991. Fitting iron and magnesium into the hydrothermal chlorite geothermometer. In: Proceedings of the Program with Abstracts, Geological Association of Canada–Mineralogical Association of Canada, Society of Economic Geologists 16, p. A62.
- Kranidiotis, P., MacLean, W., 1987. Systematic of of chlorite alteration the Phelps Dodge

- massive sulfide deposit, Matagami, Quebec. *Econ. Geol.* 82, 1898–1911.
- Laakso, K., Peter, J.M., Rivard, B., White, H.P., 2016. Short-wavce infrared spectral and geochemical characteristics of hydrothermal alteration at the Archean Izok Lake Zn-Cu-Pb-Ag volcanogenic massive sulfide deposit, Nunavut, Canada: application in exploration target vectoring. *Econ. Geol.* 111, 1223–1239.
- Lai, J.Q., Chi, G.X., Peng, S. Gc., Shao, Y.J., Yang, B., 2007. Fluid evolution in the formation of the Fenghuangshan Cu-Fe-Au deposit, Tongling, Anhui, China. *Econ. Geol.* 102, 949–970.
- Li, X.H., Li, W.X., Wang, X.C., Li, Q.L., Liu, Y., Tang, G.Q., Gao, Y.Y., Wu, F.Y., 2010. SIMS U-Pb zircon geochronology of porphyry Cu–Au–(Mo) deposits in the Yangtze River Metallogenic Belt, eastern China: magmatic response to early Cretaceous lithospheric extension. *Lithos* 119, 427–438.
- Li, J.W., Zhao, X.F., Zhou, M.F., Vasconcelos, P., Ma, C.Q., Deng, X.D., Sérgio de Souza, Z., Zhao, Y.X., Wu, G., 2008. Origin of the Tongshankou porphyry-skarn Cu-Mo deposit, eastern Yangtze craton, Eastern China: geochronological, geochemical, and Sr-Nd-Hf isotopic constraints. *Miner. Deposita* 43, 315–336.
- Li, J.W., Zhao, X.F., Zhou, M.F., Ma, C.Q., de Souza, Z.S., Vasconcelos, P., 2009. Late Mesozoic magmatism from the Daye region, eastern China: U-Pb ages, petrogenesis, and geodynamic implications. *Contrib. Miner. Petrol.* 157, 383–409.
- Ling, M.X., Wang, F.Y., Ding, X., Hu, Y.H., Zhou, J.B., Zartman, R.E., Yang, X.Y., Sun, W.D., 2009. Cretaceous ridge subduction along the lower Yangtze River Belt, Eastern China. *Econ. Geol.* 104, 303–321.
- Lv, X.B., Yao, S.Z., Lin, X.D., 1992. The geological characteristics and ore-forming mechanism of Tongshankou skarn-porphyry composite type of copper (molybdenum) ore deposit, Hubei. *Earth Sci. J. China Univ. Geosci.* 17, 171–180 in Chinese with English abstract.
- Mao, J.W., Wang, Y.T., Lehmann, B., Yu, J.J., Du, A.D., Mei, Y.X., Li, Y.F., Zang, W.S., Stein, H.J., Zhou, T.F., 2006. Molybdenite Re-Os and albite 40 Ar/39 Ar dating of Cu–Au–Mo and magnetite porphyry systems in the Yangtze River valley and metallogenic implications. *Ore Geol. Rev.* 29, 307–324.
- Miyashiro, A., Shido, F., 1985. Tschermark substitution in low- and middle-grade Pelitic Schists. *J. Petrol.* 26, 449–487.
- Neal, L.C., Wilkinson, J.J., Mason, P.J., Chang, Z., 2018. Spectral characteristics of pyritic alteration minerals as a vectoring tool for porphyry copper deposits. *J. Geochem. Explor.* 184, 179–198.
- Oliver, M.A., Webster, R., 1990. Kriging: a method of interpolation for geographical information systems. *Int. J. Geogr. Inf. Syst.* 4, 313–332.
- Pan, Y.M., Dong, P., 1999. The Lower Changjiang (Yangzi/Yangtze River) metallogenic belt, East China: intrusion- and wall rock-hosted Cu–Fe–Au, Mo, Zn, Pb, Ag deposits. *Ore Geol. Rev.* 15, 177–242.
- Pirajno, F., Zhou, T.F., 2015. Intracontinental porphyry and porphyry-skarn mineral systems in Eastern China: scrutiny of a special case “Made-in-China”. *Econ. Geol.* 110, 603–629.
- Post, J.L., Noble, P.L., 1993. The near-infrared combination band frequencies of dioctahedral smectites, micas and illites. *Clays Clay Miner.* 41, 639–644.
- Shu, Q.A., Chen, P.R., Chen, J.R., 1992. Geology of Fe-Cu Ore Deposits in Eastern Hubei Province. Press of Metallurgical Industry, Beijing, pp. 532 in Chinese with English abstract.
- Sillitoe, R.H., 2010. Porphyry Copper Systems. *Econ. Geol.* 105, 3–41.
- Thompson, A.A.B., Hauff, P.L., Robitaille, A.J., 1999. Alteration mapping in exploration: Application of shortwave infrared (SWIR) spectroscopy. *SEG Newsr.* 39, 16–27.
- Wang, Q., Zhao, Z.H., Bao, Z.W., Xu, J.F., Liu, W., Li, C.F., Bai, Z.H., Xiong, X.L., 2004. Geochimistry and petrogenesis of the Tongshankou and Yinzu Adakitic intrusive rocks and the associated porphyry copper-molybdenum mineralization in Southeast Hubei, East China. *Resour. Geol.* 54, 137–152.
- Wilkinson, J.J., Chang, Z., Cooke, D.R., Baker, M.J., Wilkinson, C.C., Inglis, S., Chen, H., Bruce Gemmill, J., 2015. The chlorite proximator: a new tool for detecting porphyry ore deposits. *J. Geochem. Explor.* 152, 10–26.
- Xia, J.L., Huang, G.C., Ding, L.X., Cheng, S.B., 2015. In situ analyses of trace elements, U-Pb and Lu-Hf isotopes in zircons from the Tongshankou Granodiorite Porphyry in Southeast Hubei Province, Middle-Lower Yangtze River Metallogenic Belt, China. *Acta Geol. Sin. (English Ed.)* 89, 1588–1600.
- Xie, G.Q., Mao, J., Li, X.W., Duan, C., Yao, L., 2011. Late Mesozoic bimodal volcanic rocks in the Jinniu basin, Middle-Lower Yangtze River Belt (YRB), East China: age, petrogenesis and tectonic implications. *Lithos* 127, 144–164.
- Xie, G.Q., Mao, J.W., Zhao, H.J., Duan, C., Yao, L., 2012. Zircon U-Pb and phlogopite ^{40}Ar - ^{39}Ar age of the Chengchao and Jinshanliao skarn Fe deposits, southeast Hubei Province, Middle-Lower Yangtze River Valley metallogenic belt, China. *Miner. Deposita* 47, 633–652.
- Xie, G.Q., Mao, J.W., Zhu, Q.Q., Yao, L., Li, Y.H., Li, W., Zhao, H.J., 2015. Geochemical constraints on Cu-Fe and Fe skarn deposits in the Edong district, Middle-Lower Yangtze River metallogenic belt, China. *Ore Geol. Rev.* 64, 425–444.
- Xie, G.Q., Mao, J.W., Li, W., Zhu, Q.Q., Liu, H.B., Jia, G.H., Li, Y.H., Li, J.J., Zhang, J., 2016. Different proportion of mantle-derived noble gases in the Cu-Fe and Fe skarn deposits: He-Ar isotopic constraint in the Edong district, Eastern China. *Ore Geol. Rev.* 72, 343–354.
- Xu, C., Chen, H.Y., Noel, W., Qi, J.P., Zhang, L.J., Zhang, S., Duan, G., 2017. Alteration and mineralization of Xinan Cu-Mo ore deposit in Zijinshan orefield, Fujian Province, and application of short wavelength infra-red technology (SWIR) to exploration. *Miner. Deposita* 36, 1013–1038 in Chinese with English abstract.
- Xu, Y.M., Jiang, S.Y., 2017. In-situ analysis of trace elements and Sr-Pb isotopes of K-feldspars from Tongshankou Cu-Mo deposit, SE Hubei Province, China: Insights into early potassiac alteration of the porphyry mineralization system. *Terra Nova* 29, 343–355.
- Yang, Z.M., Hou, Z.Q., Yang, Z.S., Qu, H.C., Li, Z.Q., Liu, Y.F., 2012. Application of short wavelength infrared (SWIR) technique in exploration of poorly eroded porphyry Cu district: a case study of Niancun ore district, Tibet. *Miner. Deposit* 31, 699–717 in Chinese with English abstract.
- Yang, K., Lian, C., Huntington, J.F., Peng, Q., Wang, Q., 2005. Infrared spectral reflectance characterization of the hydrothermal alteration at the Tuwu Cu-Au deposit, Xinjiang, China. *Miner. Deposita* 40, 324–336.
- Zhang, S.T., Chen, H.Y., Zhang, X.B., Zhang, W.F., Xu, C., Han, J.S., Chen, M., 2017. Application of short wavelength infrared (SWIR) technique to exploration of skarn deposit: a case study of Tonglvshan Cu-Fe-Au deposit, Edongnan (southeast Hubei) ore concentration area. *Miner. Deposita* 36, 1263–1288 in Chinese with English abstract.
- Zhao, X.F., Li, J.W., Ma, C.Q., 2006. ^{40}Ar - ^{39}Ar geochronology of the Tongshankou Cu (Mo) deposit in the southeastern Hubei Fe-Cu Province: implications for regional metallogeny. *Acta Geol. Sin.* 80, 861–874 in Chinese with English abstract.
- Zhou, T.F., Wang, S.W., Fan, Y., Yuan, F., Zhang, D.Y., White, N.C., 2015. A review of the intracontinental porphyry deposits in the Middle-Lower Yangtze River Valley metallogenic belt, Eastern China. *Ore Geol. Rev.* 65, 433–456.